EXPERIMENTAL INVESTIGATION OF ORIGAMI INSPIRED PHASED ARRAYS

A Thesis

By

SUMANA PALLAMPATI

Submitted to the Office of Graduate and Professional Studies of
Texas A&M University
in partial fulfillment of the requirements for the degree of

MASTER OF SCIENCE

Chair of Committee,	Gregory H. Huff
Committee Members,	Robert D. Nevels
	Jean-Francois Chamberland
	Helen Reed
Head of Department,	Miroslav M. Begovic

August 2017

Major Subject: Electrical Engineering

ABSTRACT

Origami (the art of folding) can be incorporated into antenna systems to provide compact size and low weight designs. Apart from this, the system can also provide physical reconfigurability and ease in deployment and portability. The antennas can be folded into and out of a particular shape. This will also provide a parameter in terms of folding to control the properties of the antenna system leading to a reduction in weight from external circuitry like actuators to control the antennas. But this is limited to the material constraints, complexity of design and electromagnetic performance.

Two antenna sub array systems based on origami are discussed in this thesis. The phased arrays are constructed using Microstrip patch elements and are folded based on the Miura Ori origami fold. The first is a linearly polarized 2x2 rectangular patch array operating at 2.45 GHz and the second is a circularly polarized 2x2 circular patch array operating at 3 GHz. An experimental analysis is carried out and their behavior in the intermediate folding states is studied.

From this experimental study, it is found that with the increase in the angle of folding the arrays, the impedance match becomes poor, the gain of the arrays decreases and the radiation pattern is distorted. This is due to the shielding effects of the ground plane and the decrease in the inter-element spacing. Some enabling technologies used in fabrication of origami inspired structures are 3D printing, Shape Memory Polymers and flexible conductors. Certain design considerations followed while designing a foldable array are minimizing the use of conductor on the folds.

ACKNOWLEDGEMENTS

I would like to thank my committee chair, Dr. Gregory Huff, and my committee members, Dr. R. Nevels, Dr. J. Chamberland and Dr. H. Reed for their guidance and support throughout the course of this research.

I would also like to thank the team in AFRL, Dr. Philip Buskohl, Dr. Giorgio Bazzan, Dr. Gregory Reich, Dr. Kazuko Fuchi, Dr. Edward Alyanak and Steven Seiler for their support in the project.

I would also like to thank my colleagues in the lab for their constant support and help at various stages during the course. I would thank David Grayson for helping with measurements, Steven Yeh for helping with anechoic chamber and Daniel Carry and Amrita Bal for helping with the fabrication of the array.

Thanks also go to my friends and the department faculty and staff for making my time at Texas A&M University a great experience. Finally, thanks to my mother and father for their endless encouragement throughout the time.

CONTRIBUTORS AND FUNDING SOURCES

This work was supervised by a dissertation committee consisting of Professor Dr. Gregory Huff (advisor) and Professor(s) Dr. Robert Nevels and Dr. Jean-Francois Chamberland of the Department of Electrical Engineering and Professor Dr. Helen Reed of Department of Aerospace Engineering. The work is a collaborative effort between Texas A&M University and Air Force Research Lab and is acknowledged from the support of AFOSR grant #LRIR 16RXCOR319.

NOMENCLATURE

AFRL	Air Force Research Laboratory
Ag	Silver
HFSS	High Frequency Structural Simulator
L	Length
LHCP	Left Hand Circular Polarization
QWT	Quarter Wave Transformer
RHCP	Right Hand Circular Polarization
SMP	Shape Memory Polymers
TPU	Thermoplastic Polyurethane
VNA	Vector Network Analyzer
VSWR	Voltage Standing Wave Ratio
W	Width

TABLE OF CONTENTS

Page

LIST OF FIGURES

LIST OF TABLES

1. INTRODUCTION

This project is collaboration with AFRL, Dayton, Ohio. AFRL has expertise in the area of materials, Multiphysics modelling and advanced fabrication techniques for polymers and flexible conductors. These capabilities spurred the effort to design a phased array antenna system in origami. Thus, an initial design was created and sent to Huff Research Group for measurements.

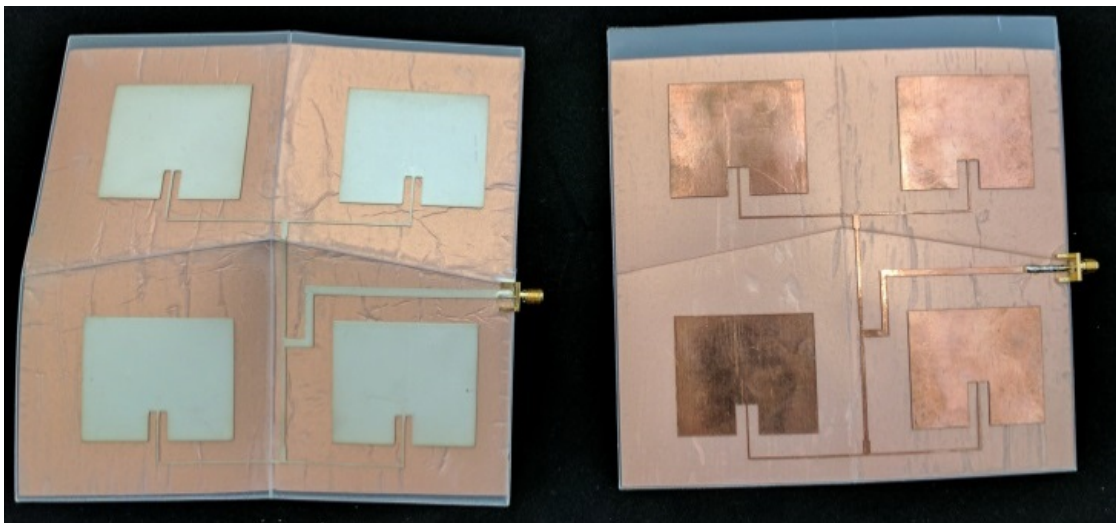

Figure 1: Fabricated Patch Antenna Array [3]

The above fabricated array is 2x2 rectangular patch array on a 1 mm thick polypropylene substrate on a miura ori unit cell. The measured radiation pattern of the arrays yielded poor results as shown below.

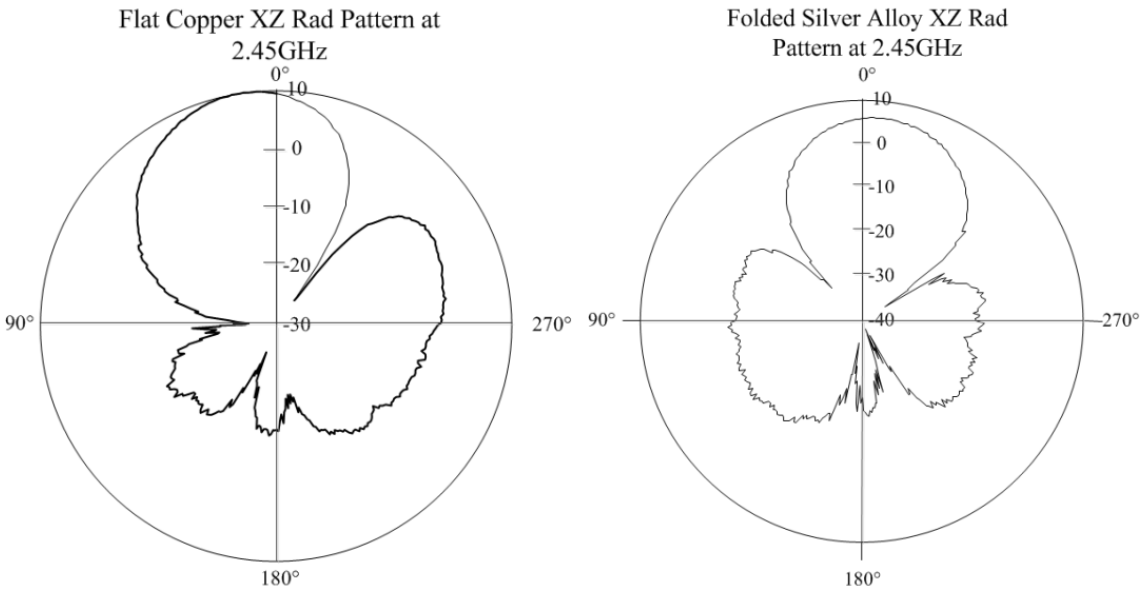

Figure 2: Measured radiation pattern for the arrays

These patterns show a very high sidelobe level. Thus, the array needed to be optimized as it was observed that the feed network impedances were not considered appropriately. Thus, the design was optimized for the correct impedances and that led to the building of a more robust and functional antenna array system with a circular patch element operating in sum and difference configuration with circular polarization. The use of circular polarization eliminates the need to study the polarization changes during intermediate folding states.

This thesis aims to study the impact of folding on the impedance and radiation behavior of the phased array. It also discusses the design considerations to be taken into account while designing an origami based phased array. Also, the enabling technologies required to fabricate and operate the phased array are discussed in brief.

2. EMERGING TECHNOLOGIES FOR FABRICATION

2.1. INTRODUCTION

Smart materials are gaining lot of interest recently as they provide more flexibility in design and allow for studying different behavior and properties. These materials find applications in different fields like medicine for implants in minimally invasive surgery, space for easy deployment of large solar panels, electronics for flexible assembly and packaging to name a few. They are being used in electromagnetics to study adaptive antenna systems based on different physical states. One of the applications is in origami based structures. Examples of smart materials are shape memory polymers (SMP) and flexible conductors.

2.2. SHAPE MEMORY POLYMERS

Shape memory polymers change their shape when an external stimulus is applied. The stimulus can either be heat or light. The most widely used stimulus is heat.

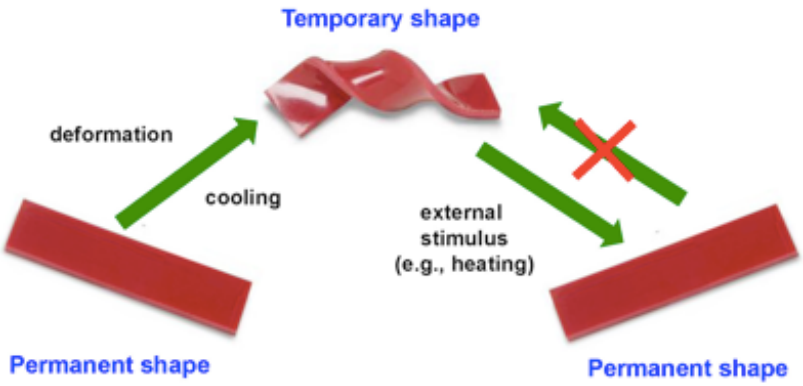

Source: http://www-2.unipv.it/compmech/polymers.html

Figure 3: Shape Memory Effect based on heat

By deforming the permanent shape, a temporary shape can be achieved. This can be done by cooling and applying force. The temporary shape can be changed to the permanent shape by heating. The change in shape is achieved using the molecular network. The molecular network has netpoints. These netpoints determine the permanent shape and are usually the covalent or ionic bonds. As the external stimulus is applied, the reversible covalent bonds are formed so that when the stimulus is removed, the permanent shape can be obtained.

The light induced shape memory effect uses light with different wavelengths as stimulus. In this case, the molecular bonds are sensitive to light. Irradiating the polymer with a particular wavelength of light causes the creation of new bonds (netpoints). These bonds determine the temporary shape of the polymer. To retrieve the permanent shape, the polymer is irradiated with a light of different wavelength. This causes the cleavage of the netpoints formed for the temporary shape (photocleaving). This process is illustrated by following figure.

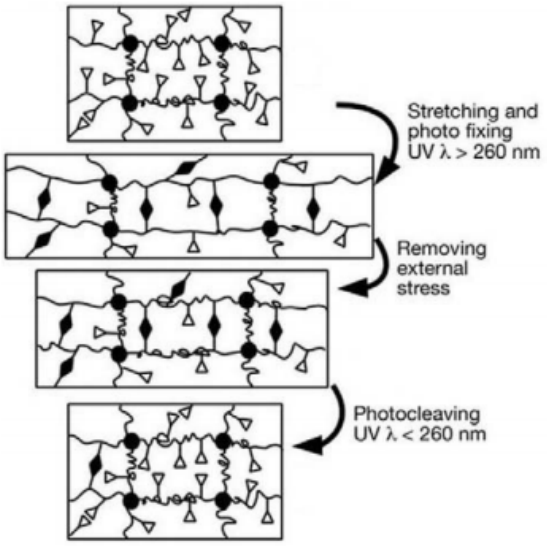

Figure 4: Light induced shape memory effect [22]

2.3. FLEXIBLE CONDUCTORS AND FABRICATION

Flexible conductors are gaining a lot of importance with the rise in popularity of wearable technology and flexible electronics. These flexible conductors are being manufactured as ink which can be easily fed into a 3D printer or laser printer and thus, can be printed on a variety of surfaces. One example of such an ink is Ag TPU. This is synthesized using Ag nanoparticles with TPU composite. The origami rectangular patch array discussed in this thesis has two fabricated versions, one with copper tape and another with Ag TPU ink.

3D printing is widely being used with shape memory polymers and flexible conductors. If the ink is particulate or liquid, inkjet and laser printers are also being used for fabrication of these structures.

3. BACKGROUND AND LITERATURE REVIEW

3.1. MICROSTRIP PATCH ANTENNAS

Microstrip patches are printed circuit low profile, narrowband antennas which are easy to design. They can be designed on different kind of substrates and in different shapes. The most common shapes are rectangular and circular patch. There are different feeding techniques like probe feeding and edge feeding. The shape and type of feeding of the antenna can be selected based on application.

3.2. RECTANGULAR PATCH

Rectangular Patches are the most widely used patch antennas. The length (L) of the antenna is of resonant length (half wavelength). A typical rectangular Microstrip patch is shown below. [2]

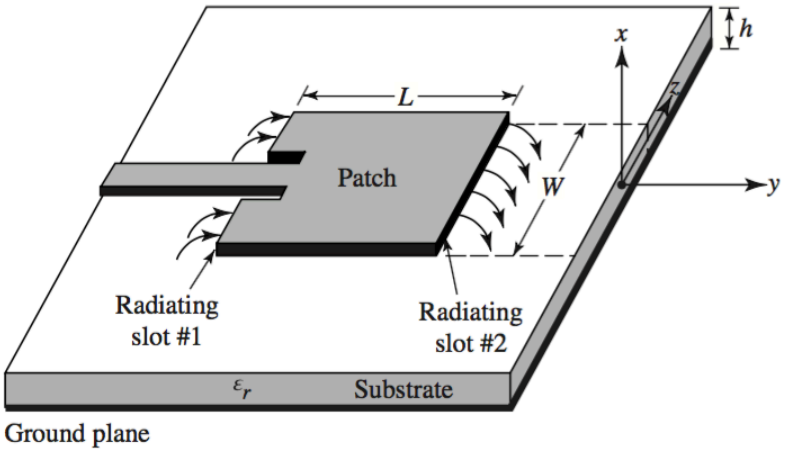

Figure 5: Rectangular Microstrip Patch [2]

Patch Antenna consists of a metallic patch (length L and width W), a dielectric substrate of height h and a metallic ground plane. The signal is fed using a Microstrip line or a coaxial feed.

The Microstrip patch can be modeled using a transmission line model and a cavity model. The cavity model considers the patch as having two slots of width W and height h. These slots are separated by length L of the patch. Thus, the slots act as a two element uniform linear phased array. To find the radiation pattern of the patch, the pattern function of one slot is calculated and it is then multiplied by the array factor. The current through each slot is given by $M_s = -2\hat{n}\times E_a$, where E_a is the electric field of the slot.

The electric field of one slot is given by

$$E_r \approx E_\theta \approx 0 \tag{2.1}$$

$$E_\phi = +j\frac{k_0 hWE_0 e^{-jk_0 r}}{2\pi r}\left\{sin\theta.\frac{\sin(\frac{k_0 h}{2}.sin\theta.cos\phi)}{\frac{k_0 h}{2}.sin\theta.cos\phi}.\frac{\sin(\frac{k_0 W}{2}.cos\theta)}{\frac{k_0 W}{2}.cos\theta}\right\} \tag{2.2}$$

The array factor is given by

$$(AF)_y = 2\,cos\left(\frac{k_0 L_e}{2}\,sin\theta\,sin\phi\right) \tag{2.3}$$

Thus combining the above equations, the expressions for radiated fields for E – plane ($\theta = 90°, 0° \le \phi \le 90°\ and\ 270° \le \phi \le 360°$) and H – plane ($\phi = 0°, 0° \le \theta \le 180°$ are given by

$$E_\phi^t = +j\frac{k_0 hWE_0 e^{-jk_0 r}}{\pi r}\left\{\frac{\sin(\frac{k_0 h}{2}cos\phi)}{\frac{k_0 h}{2}cos\phi}\right\}cos\left(\frac{k_0 L_e}{2}\,sin\phi\right), \tag{2.4}$$

$$E_\phi^t = +j\frac{k_0 hWE_0 e^{-jk_0 r}}{\pi r}\left\{sin\theta.\frac{\sin(\frac{k_0 h}{2}.sin\theta)}{\frac{k_0 h}{2}.sin\theta}.\frac{\sin(\frac{k_0 W}{2}.cos\theta)}{\frac{k_0 W}{2}.cos\theta}\right\}, \text{ respectively.} \tag{2.5}$$

3.3. DESIGN OF RECTANGULAR PATCH

To design a rectangular patch, the dielectric constant of substrate ϵ_r, height of the substrate h and the operating frequency f_r must be known. Then the length L and width W of the patch can be calculated as follows.

$$\epsilon_{reff} = \frac{\epsilon_r+1}{2} + \frac{\epsilon_r-1}{2}\left[1 + 12\frac{h}{W}\right]^{-1/2} \text{ for } W/h \geq 1 \tag{2.6}$$

$$\frac{\Delta L}{h} = 0.412\frac{(\epsilon_{reff}+0.3)\left(\frac{W}{h}+0.264\right)}{(\epsilon_{reff}-0.258)\left(\frac{W}{h}+0.8\right)} \tag{2.7}$$

$$W = \frac{1}{2f_r\sqrt{\mu_0\epsilon_0}}\sqrt{\frac{2}{\epsilon_r+1}} \tag{2.8}$$

$$L = \frac{1}{2f_r\sqrt{\epsilon_{reff}}\sqrt{\mu_0\epsilon_0}} - 2\Delta L \tag{2.9}$$

Where ϵ_{reff} is the effective dielectric constant of the substrate, μ_0 is the permeability of free space and $\epsilon_0$is the permittivity of free space.

Microstrip patch is fed by either a microstrip feed line with an inset or with a coaxial probe. To find the location y_0 of the probe or the recessed distance from the edge of the patch (along W) for a microstrip feed line, the following equation is used. The input impedance of a microstrip patch at resonance is real.

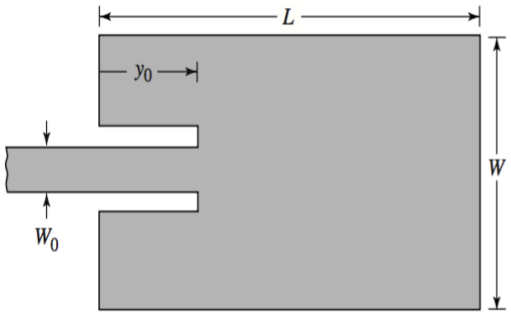

Figure 6: Microstrip Patch with inset feed [2]

$$R_{in}(y = y_0) = \frac{1}{2(G_1 \pm G_{12})}\left[\cos^2\left(\frac{\pi}{L}y_0\right) + \frac{G_1^2 + B_1^2}{Y_c^2}\sin^2\left(\frac{\pi}{L}y_0\right) - \frac{B_1}{Y_c}\sin\left(\frac{2\pi}{L}y_0\right)\right] \quad (2.10)$$

Which reduces to

$$R_{in}(y = y_0) = \frac{1}{2(G_1 \pm G_{12})}\left[\cos^2\left(\frac{\pi}{L}y_0\right)\right] \quad (2.11)$$

as $\frac{G_1}{Y_c} \ll 1$ and $\frac{B_1}{Y_c} \ll 1$ for typical microstrips.

Where

$$G_1 = \begin{cases} \frac{1}{90}\left(\frac{W}{\lambda_0}\right)^2 & W \ll \lambda_0 \\ \frac{1}{120}\left(\frac{W}{\lambda_0}\right) & W \gg \lambda_0 \end{cases} \quad (2.12)$$

$$G_{12} = \frac{1}{120\pi^2}\int_0^{\pi}\left[\frac{\sin\left(\frac{k_0 W}{2}\cos\theta\right)}{\cos\theta}\right]^2 J_0(k_0 L\sin\theta)\sin^3\theta d\theta \quad (2.13)$$

$$Y_c = 1/Z_c \quad (2.14)$$

$$Z_c = \begin{cases} \frac{60}{\sqrt{\epsilon_{reff}}} ln\left[\frac{8h}{W_0} + \frac{W_0}{4h}\right], & \frac{W_0}{h} \leq 1 \\ \frac{120\pi}{\sqrt{\epsilon_{reff}}\left[\frac{W_0}{h} + 1.393 + 0.677\ln\left(\frac{W_0}{h} + 1.444\right)\right]}, & \frac{W_0}{h} > 1 \end{cases} \quad (2.15)$$

3.4. CIRCULAR PATCH

Circular patch or disk is another common type of microstrip patch. It consists of a circular metallic sheet with radius a, on top of a substrate with height h and dielectric constant ϵ_r. The bottom of the substrate is covered with a ground plane. It is shown in the following figure. The feeding mechanisms are similar to the microstrip patch namely the coaxial probe feed and the inset feed. [2]

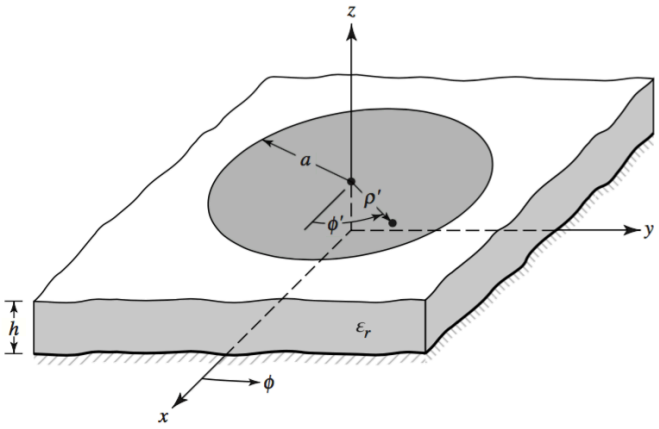

Figure 7: Circular Patch Antenna [2]

The circular patch can be analyzed using the cavity model. The cavity is represented by a PMC in cylindrical coordinates and the top and bottom are PEC (patch and the ground plane respectively). Again the current in the cavity is given by $M_s = -2\hat{n}\times E_a$ and assuming the circular patch to be a circular loop, the radiation equations are given as follows.

For E – plane ($\phi = 0°, 180°, 0° \leq \theta \leq 90°$), $E_\phi = 0$ and

$$E_\theta = j\frac{k_0 a_e V_0 e^{-jk_0 r}}{2r}[J'_{02}] \tag{2.16}$$

For H – plane ($\phi = 90°, 270°, 0° \leq \theta \leq 90°$), $E_\theta = 0$ and

$$E_\phi = j\frac{k_0 a_e V_0 e^{-jk_0 r}}{2r}[\cos\theta J_{02}] \tag{2.17}$$

Where a_e is the effective radius of the patch, $V_0 = hE_0 J_1(ka_e)$ at $\phi' = 0$, $J'_{02} = J_0(k_0 a_e \sin\theta) - J_2(k_0 a_e \sin\theta)$ and $J_{02} = J_0(k_0 a_e \sin\theta) + J_2(k_0 a_e \sin\theta)$. J_0 and J_2 are Bessel functions.

3.5. DESIGN OF CIRCULAR PATCH

To design a circular patch, the operating frequency f_r in Hz, the dielectric constant of the substrate ϵ_r and the height of the substrate h in cm are specified. Then the radius of the circular patch a is given by the following equation. [2]

$$a = \frac{F}{\left\{1+\frac{2h}{\pi\epsilon_r F}\left[ln\left(\frac{\pi F}{2h}\right)+1.7726\right]\right\}^{1/2}} \tag{2.18}$$

where

$$F = \frac{8.791\times10^9}{f_r\sqrt{\epsilon_r}} \tag{2.19}$$

The input impedance of a circular patch is analogous to the rectangular patch and it is real. The circular patch can also be fed similar to the rectangular patch. A probe feed or an inset feed can be used. The resistance of the patch is constant along a particular ρ. Thus, the patch can be fed from any direction. To find the location of the inset ρ_0, the following equations are used.

$$R_{in}(\rho' = \rho_0) = \frac{1}{G_t}\frac{J_1^2(k\rho_0)}{J_1^2(ka_e)} \tag{2.20}$$

which can be reduced to

$$R_{in}(\rho' = \rho_0) = R_{in}(\rho' = a_e)\frac{J_1^2(k\rho_0)}{J_1^2(ka_e)} \tag{2.21}$$

$$R_{in}(\rho' = a_e) = \frac{1}{G_t} \tag{2.22}$$

where a_e is the effective radius of the patch and G_t is the total conductance and is equal to the sum of radiation conductance G_{rad}, conductance due to ohmic losses G_c and dielectric losses G_d and is given by

$$G_t = G_{rad} + G_c + G_d \tag{2.23}$$

The radiation conductance, conduction due to ohmic losses and dielectric losses are represented as

$$G_{rad} = \frac{(k_0 a_e)^2}{480} \int_0^{\pi/2} [J_{02}'^2 + \cos^2\theta J_{02}^2] \sin\theta \, d\theta \tag{2.24}$$

$$G_c = \frac{\varepsilon_{m0}\pi(\pi\mu_0 f_r)^{-3/2}}{4h^2\sqrt{\sigma}} [(ka_e)^2 - m^2] \tag{2.25}$$

$$G_d = \frac{\varepsilon_{m0}\tan\delta}{4\mu_0 h f_r} [(ka_e)^2 - m^2] \tag{2.26}$$

where $\varepsilon_{m0} = 2$ for $m = 0$, $\varepsilon_{m0} = 1$ for $m \neq 0$ and f_r is the resonant frequency of the $mn0$ mode.

3.6. CIRCULAR POLARIZATION IN MICROSTRIP PATCHES

Circular polarization (CP) is useful as the antenna can detect or receive any kind of polarization. Circular polarization is represented in two polarizations namely co-polarization and cross-polarization. Co-polarization refers to the direction of polarization in which the antenna is supposed to radiate and cross-polarization refers to the orthogonal direction to the co-polarization. Left Hand Circular Polarization (LHCP) and Right Hand Circular Polarization (RHCP) are the two directions in which the electric field can rotate. [2]

Circular polarization can be achieved in microstrip patches in different ways. One way is by a single feed. Circular polarization is achieved by introducing asymmetry so that two modes can be excited with a 90° phase difference between them. The introduction of the asymmetry creates inductive and capacitive effects. The resonant frequency is chosen between the two operating modes. If the two modes are excited in

such a manner that one leads by 45° and the other lags by 45°, circular polarization can be created. The asymmetry is achieved perturbations on the edges or having narrow slots in the middle inclined at an angle.

In rectangular patches, this can be achieved by perturbing the opposite corners of the patch, or by feeding the patch in the corner or by introducing a thin a slot in the middle of the patch inclined at 45°. This slot helps in rotating the incoming electric field in a circular direction. The patch is made nearly square for circular polarization. In circular patches, this can be achieved by either making the patch slightly elliptical and adding tabs at 45° from the major axis or by introducing a thin slot in the center of the patch inclined at an angle of 45°. In addition, it can also be achieved by perturbing the patch across its diameter. The direction of the slot i.e. whether it is inclined towards $+45°$ or $-45°$ indicates whether the patch is in RHCP or LHCP co-polarization. The following figures show circular polarization in patches.

The second way is by dual feeding the patch by placing both the feeds at 90° w.r.t each other and the signals should be different in phase by 90°. The dual feed can be applied to both types of patches. The 90° phase difference between the input signals can be achieved by using a hybrid coupler or a phase shifter. [2]

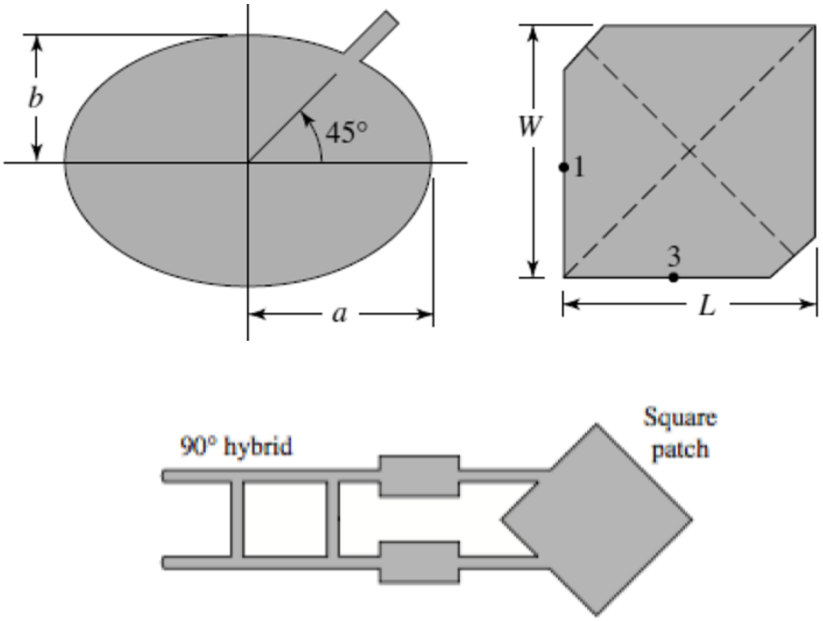

Figure 8: Circular Polarization in Patches – Elliptical Patch, Square Patch with trimmed corners and Dual fed Patch for circular polarization with hybrid coupler [2]

3.7. FEED NETWORK IN PATCH ARRAYS

Patch Arrays can be fed using two feeding methods namely a corporate feed or a series feed. The corporate feed network is based on splitting the power and also impedance matching the load i.e. patch element with 50 Ω input impedance. This is achieved using single or multiple quarter wave transformer sections. The series feed is easily implemented monolithically but the corporate feed is more widely used. [2]

3.8. MIURA ORI FOLD IN ORIGAMI

Miura Ori is a typical type of fold in origami (the art of paper folding). This fold is used on the substrate to fold the patch array. This type of fold is selected for studying

as the geometry of the well documented and this fold has been utilized for deployment of solar panels in space. It is a form of tessellation in which four individual parallelograms are folded in such a manner that on one side there is a mountain fold and on the other side there is a crest fold. This unit cell repeats in both the x and y directions and thus forms a tessellation. The geometry of the unit cell is discussed as follows. [5]

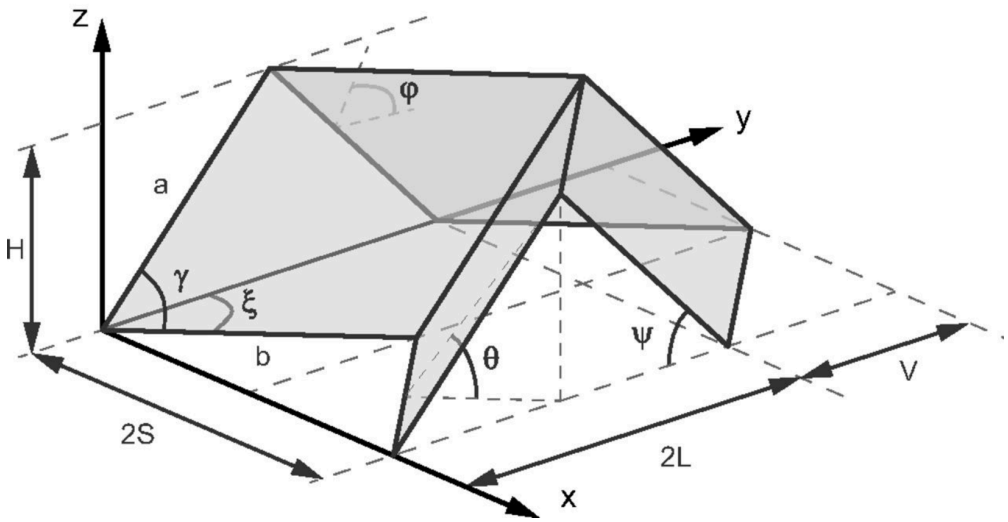

Figure 9: Miura Ori Unit Cell [5]

The unit cell consists of four parallelograms. Each parallelogram has dimensions $a \times b$ where a is the width and b is the length. The angle between a and b is γ. The angle of the fold is given by θ, which lies in the range between 0° and 90°. For the above diagram, the different parameters namely the outer dimensions H, S, L and V and the angles ξ, ψ and φ are given by the following equations.

$$H = a \sin\theta \sin\gamma \tag{2.26}$$

$$S = b \frac{\cos\theta \tan\gamma}{\sqrt{1+\cos^2\theta \tan^2\gamma}} \tag{2.27}$$

$$L = a\sqrt{1 - \sin^2\theta \sin^2\gamma} \tag{2.28}$$

$$V = b\frac{1}{\sqrt{1+\cos^2\theta\tan^2\gamma}} \tag{2.29}$$

$$\tan\xi = \cos\theta\tan\gamma \tag{2.30}$$

$$\sin\psi = \sin\theta\sin\gamma \tag{2.31}$$

$$\cos\gamma = \cos\xi\cos\psi \tag{2.32}$$

$$\sin\varphi = \sin\xi / \sin\gamma \tag{2.33}$$

3.9. UNIFORM LINEAR ARRAYS

Phased arrays refer to a number of individual antenna elements separated by a distance d and each element of the array is fed with a progressive phase shift to achieve the desired radiation pattern. The total field of the array is given by the field of the single element multiplied by a term that depends on the distance of separation of the elements d and the phase with which they are fed. This term is known as the array factor (AF).

Linear Arrays are one-dimensional arrays. The progressive phase shift of the arrays follows a particular distribution. The distribution is selected based on the desired properties of the array. For uniform linear arrays, the progressive phase shift is uniform. [2]

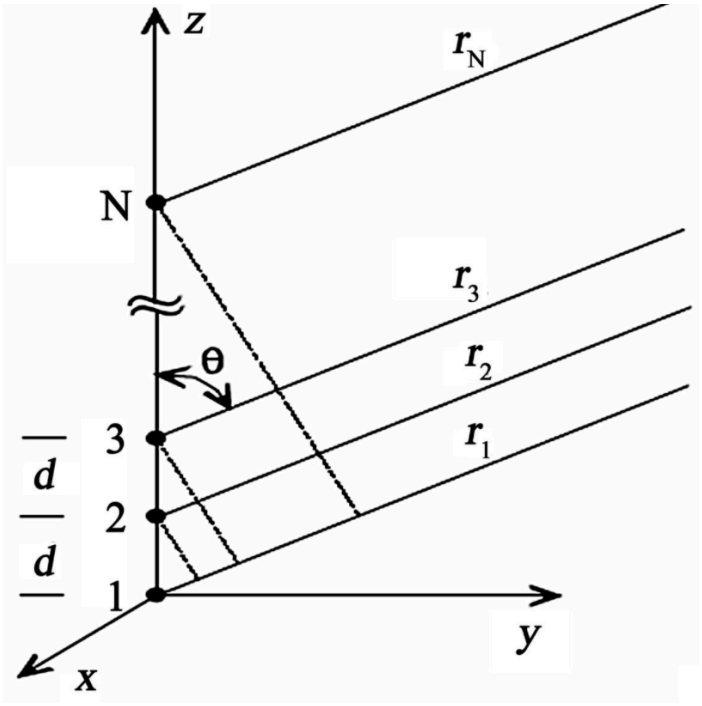

Figure 10: z directed uniform linear array [2]

The array factor for the above uniform linear array is given by

$$AF = \frac{\sin\left(\frac{N}{2}\psi\right)}{\sin\left(\frac{1}{2}\psi\right)} \tag{2.34}$$

Where $\psi = kd\cos\theta + \beta$ and β is the progressive phase shift between the elements.

3.10. UNIFORM PLANAR ARRAYS

Planar arrays are two-dimensional arrays. The elements are placed in a two-dimensional matrix. A uniform planar array has a uniform progressive phase shift.

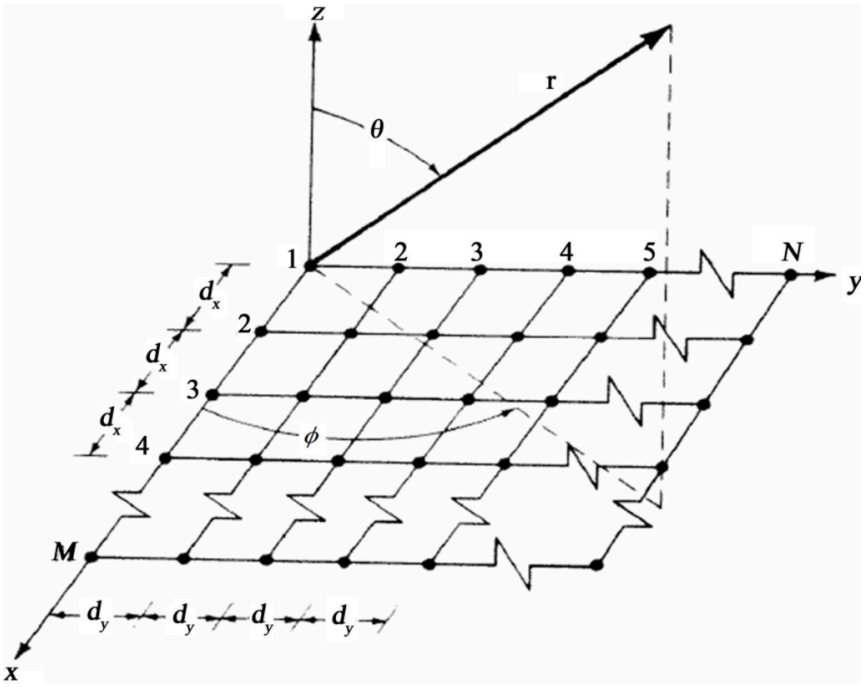

Figure 11: Uniform Planar Array [2]

The array factor of the above array is found by considering the element factor of the individual elements and then multiplying it with the linear array factor along x and y-axis. The elements are spaced at distance d_x along x-axis and d_y along y-axis.

The array factor of a $M \times N$ two-dimensional array is given by

$$AF = \left\{\frac{1}{M}\frac{\sin\left(\frac{M}{2}\psi_x\right)}{\sin\left(\frac{\psi_x}{2}\right)}\right\}\left\{\frac{1}{N}\frac{\sin\left(\frac{N}{2}\psi_y\right)}{\sin\left(\frac{\psi_y}{2}\right)}\right\} \tag{2.35}$$

where

$$\psi_x = kd_x \sin\theta \cos\phi + \beta_x \tag{2.36}$$

$$\psi_y = kd_y \sin\theta \cos\phi + \beta_y \tag{2.37}$$

β_x and β_y are the progressive phase shifts in x and y-axis respectively.

4. RECTANGULAR PATCH ARRAY ON MIURA ORI[1]

4.1. INTRODUCTION

After measuring the fabricated patch array sent by AFRL, the measured results were not in accordance with the expectation. Thus, there was a need to optimize the array to yield accurate results. So the patch array and the patch element were redesigned.

4.2. RECTANGULAR PATCH ELEMENT

The rectangular patch element is designed at a frequency of 2.45 GHz on a polypropylene substrate with a dielectric constant of 2.1. The height of the substrate is 1mm. The dimensions of the patch are $W = 47.5\ mm$ and $L = 40.7\ mm$. It is matched to a 100 Ω line using an inset feed. The length of the inset is 8.7 mm. This patch is designed using eqns. (2.6) – (2.9) and is modeled in Ansys HFSS. The HFSS model is shown below.

1 Part of this chapter has been accepted in proceedings of IEEE AP-S 2017. The original citation is: Steven R. Seiler et.al, Physical Reconfiguration of an Origami-Inspired Deployable Microstrip Patch Antenna Array, IEEE AP-S 2017.

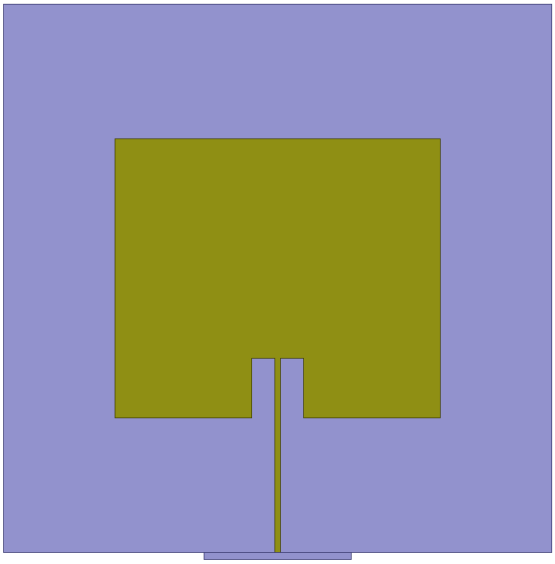

Figure 12: Rectangular Patch Element modeled in HFSS

The simulated result of radiation pattern and VSWR of the patch is shown below. The pattern is taken for xz- and yz- cut planes. The gain of the patch is observed to be 7.07 dB. The VSWR is 1 at 2.45 GHz indicating that the patch is matched.

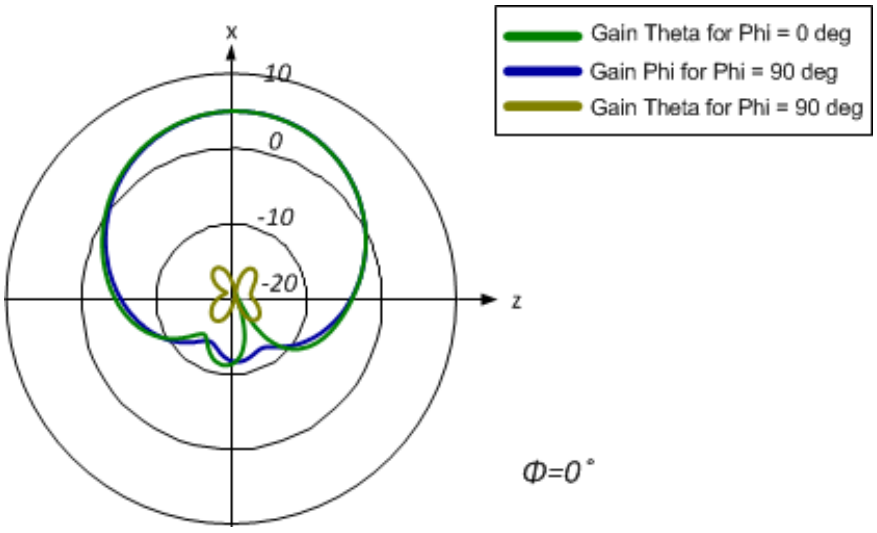

Figure 13: Simulated Radiation Pattern

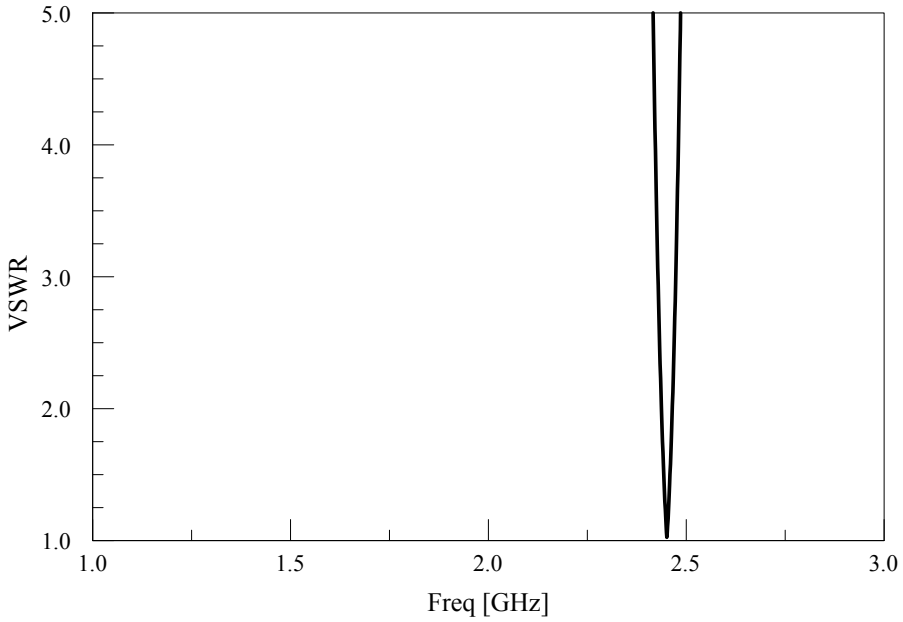

Figure 14: Simulated VSWR

4.3. THE FEED NETWORK

The feed network has been designed to impedance match the 100 Ω impedance of the patch to the 50 Ω feed line. They are matched using quarter wave transformer segments of 70.7 Ω. The widths of the microstrip lines of the feed network have been determined using online calculators. The widths are tabulated below.

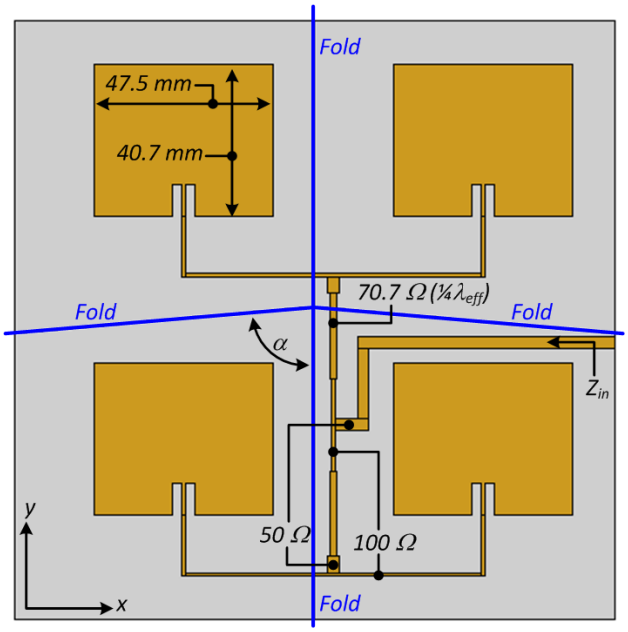

Figure 15: Patch Array on Miura Ori with the feed network [3]

Impedance (Ω)	Dimensions (mm)
50	3.08 (width)
100	0.896 (width)
70.7	1.76 (width)
70.7	22.722 (length of QWT)

Table 1: Dimensions of the Feed Network for rectangular patch array

4.4. PATCH ARRAY ON MIURA ORI FOLD

Once the element is designed, an 2×2 element sub-array is designed on polypropylene substrate. Each parallelogram of the miura ori unit cell has dimensions of $80mm\times80mm$. The acute angle α between the two sides is $85°$. The array on the miura

fold is shown. This array has been simulated in Comsol Multiphysics. The array bent at various angles is shown.

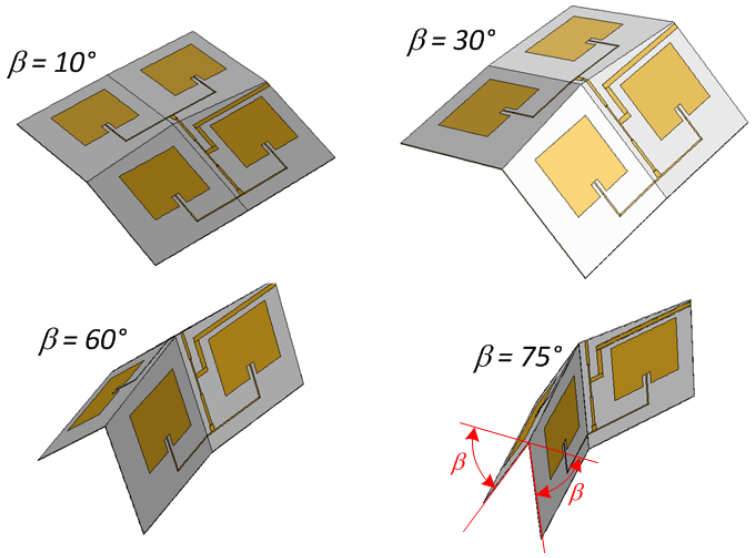

Figure 16: The Array bent at different angles [3]

4.5. RESULTS AND DISCUSSION

The simulated results of S_{11} in dB and radiation pattern of the array are shown below. It is observed that as the bending in the array increases, the gain in the pattern decreases and the beamwidth increases. The pattern becomes distorted. The S_{11} results indicate that as the angle of bending increases, the impedance match becomes poor due to additional loading. At a 90° bend angle, i.e. a completely bent state, the pattern is completely distorted and the impedance match is completely detuned. The results for S_{11} are taken for bend angles of β = 0°, 10°, 30°, 60°, and 75°. The results for the radiation pattern are taken at bend angles of β = 0°, 10°, 30° and 60°.

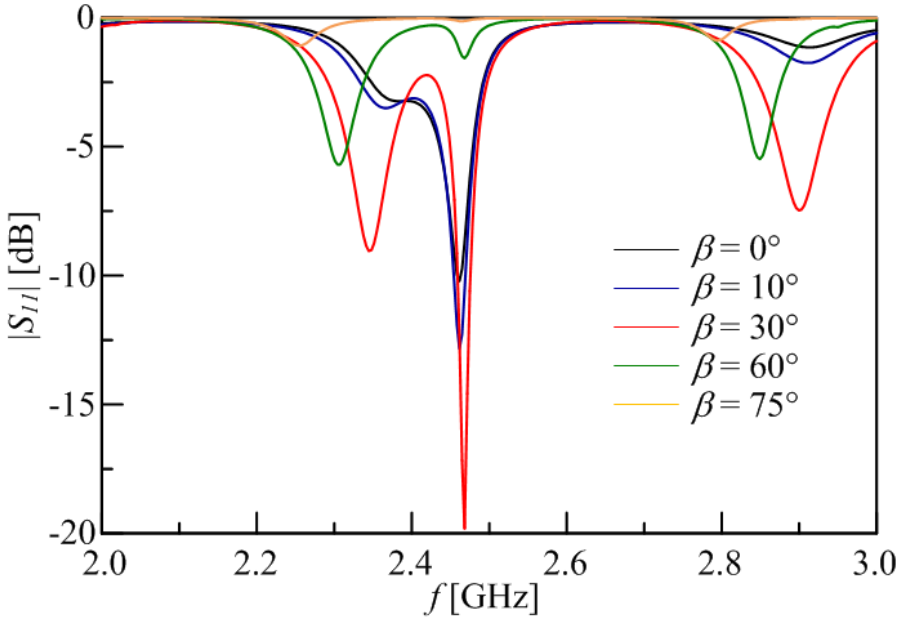

Figure 17: Simulated S_{11} in dB at various bend angles [3]

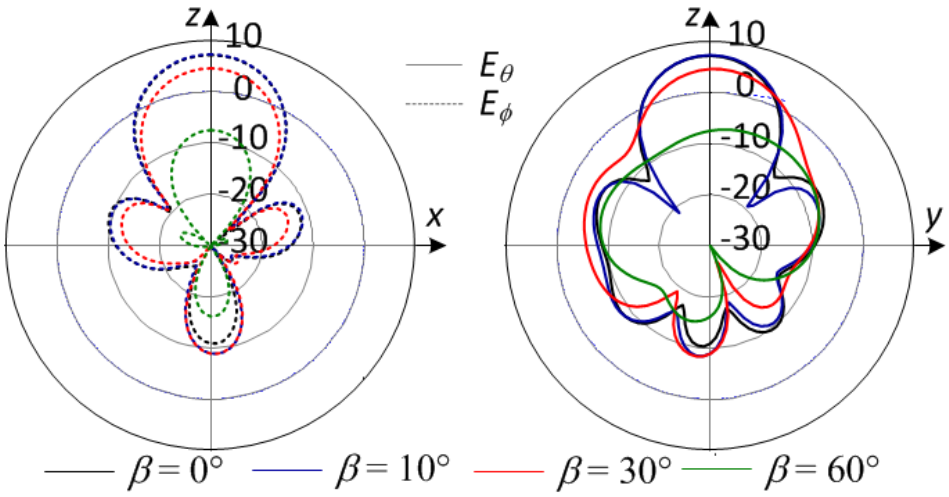

Figure 18: Simulated co- and cross-polarization radiation pattern at different bend angles for xz and yz cut planes [3]

4.6. FABRICATION

The patch array has been fabricated on a 1mm thick polypropylene substrate with a dielectric constant of 1mm. The metal on one prototype is a flexible conductor (Ag TPU) and the metal on the second prototype is fabricated by using laser etching on copper tape. The fabricated arrays are shown below.

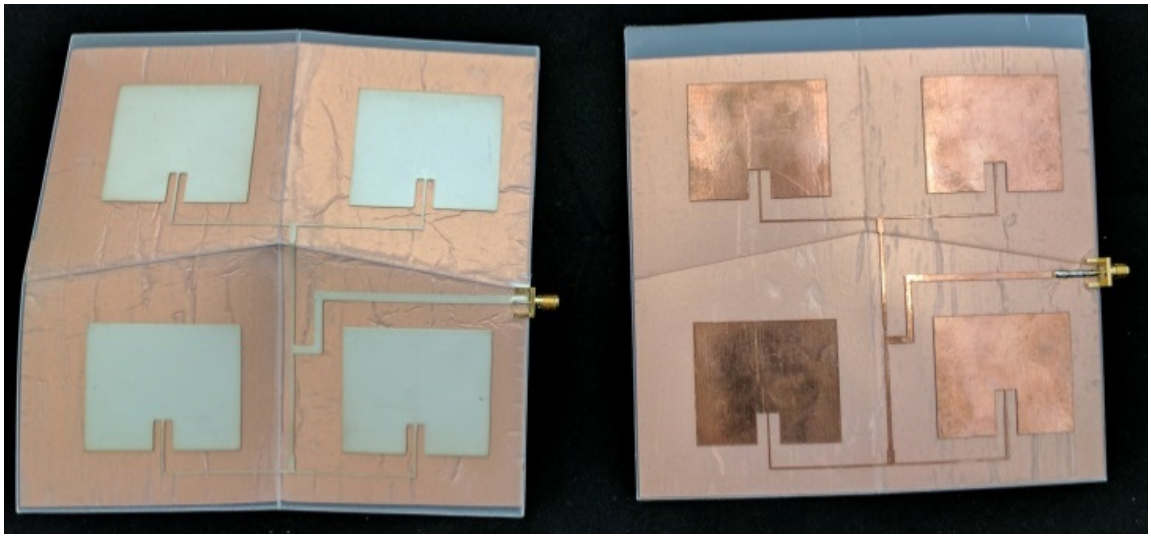

Figure 19: Fabricated Patch Array (left) Flexible Conductor and (right) Laser Etched Copper [3]

5. CIRCULAR PATCH ARRAY ON MIURA ORI

5.1. INTRODUCTION

The rectangular patch array discussed in the previous chapter is linearly polarized and has no pattern reconfigurability. To improve the functionality of the patch array, a new design along the lines of the rectangular patch array is designed. This constitutes a circularly polarized circular patch array with sum and difference patterns. Circular polarization is necessary because the polarization changes as the array folds. Circular polarization enables the reception of the signal in any polarization.

5.2. THE CIRCULAR PATCH ELEMENT

The circular patch is designed on Rogers RTD Duroid 5880 with a dielectric constant of 2.2. The height of the substrate is 62 mils. The patch element is left hand circularly polarized (LHCP) and single fed. To implement the circular polarization, a narrow elliptical slot is cut in the middle of the patch. The slot is inclined at an angle of $-45°$. This helps in rotating the incoming electric field. The dimensions of the patch are calculated using eqns. (2.18) – (2.22).

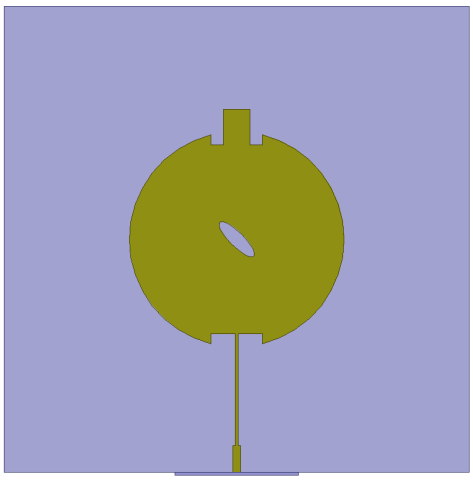

Figure 20: Patch Element in HFSS

The patch is impedance matched to 100 Ω using a combination of inset, quarter wave transformer and an open circuit stub. It is desired to use an inset feed. But, using a deep inset into the patch disrupts the circular polarization. Moreover, the inset length of 2.3 mm into the patch puts the 3 GHz point on the Smith Chart onto the (1,0) circle. Thus, the resistance is matched but the reactance is not. In order to match the reactance, an open circuit stub is placed at the opposite side of the feed. This stub also helps in circular polarization as it creates symmetry in the design. The dimensions of the design are tabulated below. This patch is modeled in Ansys HFSS.

Parameter	Dimensions (mm)
Radius	18.5
L of inset	2.3
W of inset	8.9
L of stub	6.1
W of stub	4.5
W of 100 Ω feed	1.4114
W of QWT	0.465
L of QWT	19.21
L of slot	8.2
W of slot	2.46

Table 2: Dimensions of the Circular Patch Element

5.3. FABRICATION AND MEASUREMENTS

The patch element is fabricated on a 62 mil RT Duroid 5880. The radiation pattern at 3GHz of the simulated and measured results is shown below. The patch has a gain of 7.74 dB. The LHCP and RHCP pattern have a difference of 14.645 dB.

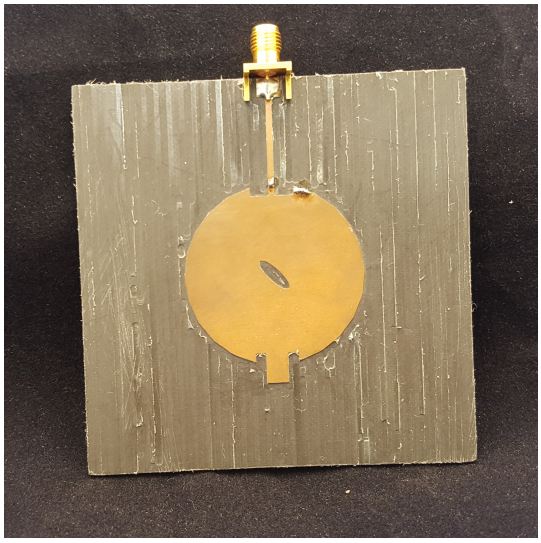

Figure 21: Fabricated Patch Element on Duroid

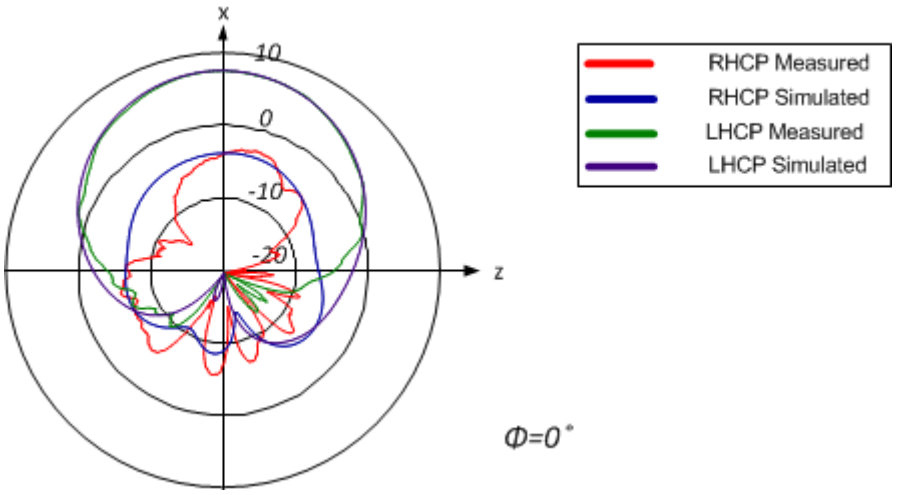

Figure 22: Radiation Pattern for the Circular Patch Element

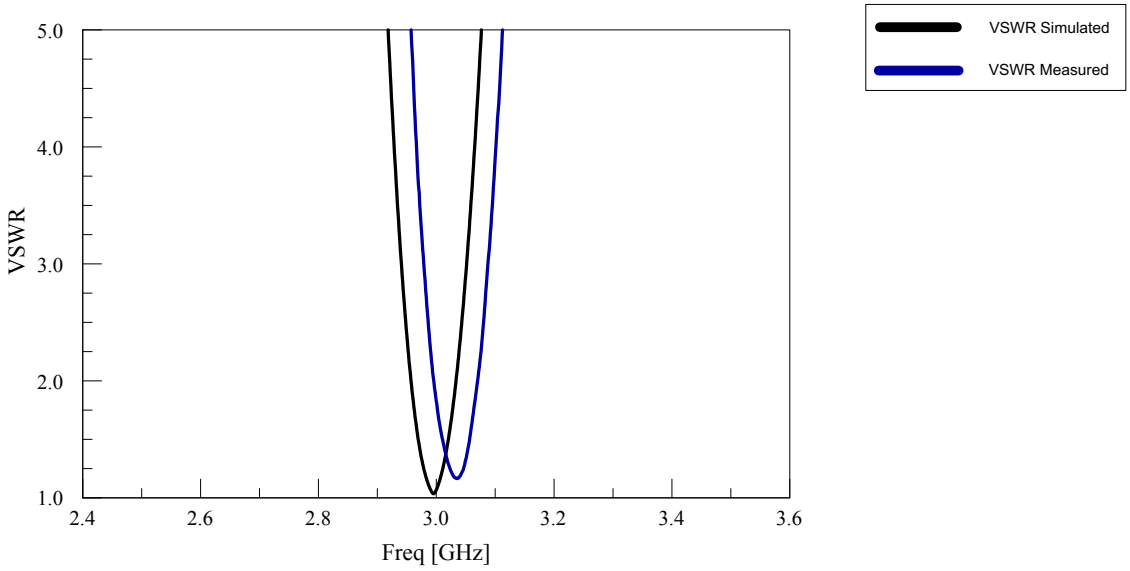

Figure 23: VSWR for the Circular Patch Element

The simulated and measured VSWR results are close and they are close to 1 indicating a good match at 3 GHz.

5.4. FLAT 2X2 PATCH ARRAY ON DUROID

The above patch element is used to form a 2x2 sub-array on Duroid 5880 substrate. The feed network involves a 50 Ω line splitting into two 100 Ω lines and thus eventually feeding the four patch elements. When no phase shift is provided, a difference (endfire) pattern is observed whereas providing a 180° phase shift to two adjacent elements gives a sum (broadside) pattern. The uniqueness of the array is that the individual elements are circularly polarized and the sub-array is also circularly polarized. The dimensions of the feed network are tabulated below.

Parameter	Dimension (mm)
W of 50 Ω	4.5
W of 100 Ω	1.4114
L of 180˚line	37.7

Table 3: Dimensions of the Feed Network for circular patch array

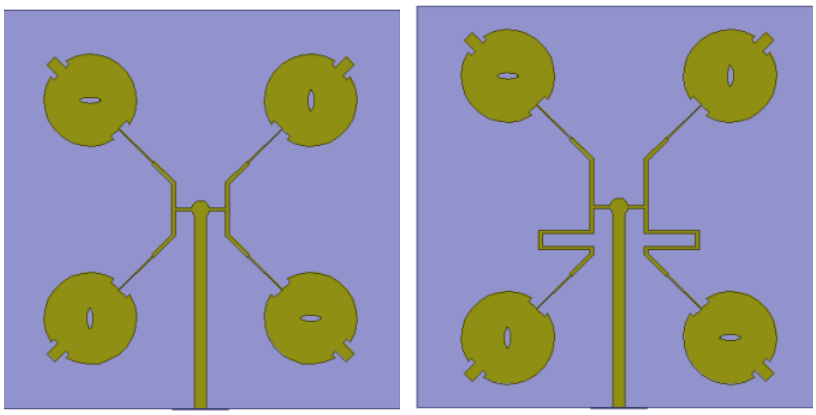

Figure 24: Patch Array model on Duroid in HFSS (left) Difference Configuration (right) Sum Configuration

5.5. SIMULATION AND MEASUREMENTS

The array has dimensions of 160 mm x 160 mm. It is fabricated in the milling machine. The VSWR measurements are taken on the Agilent Vector Network Analyzer and the radiation pattern measurements are taken in the Anechoic Chamber. To create a circular polarization receiver, the horizontal and vertical polarization feeds in the chamber are fed by signals with 90° phase shift between them. This is achieved using a hybrid coupler. The Network Analyzer is calibrated using a 1 port Short, Open, Load Calibration (SOL).

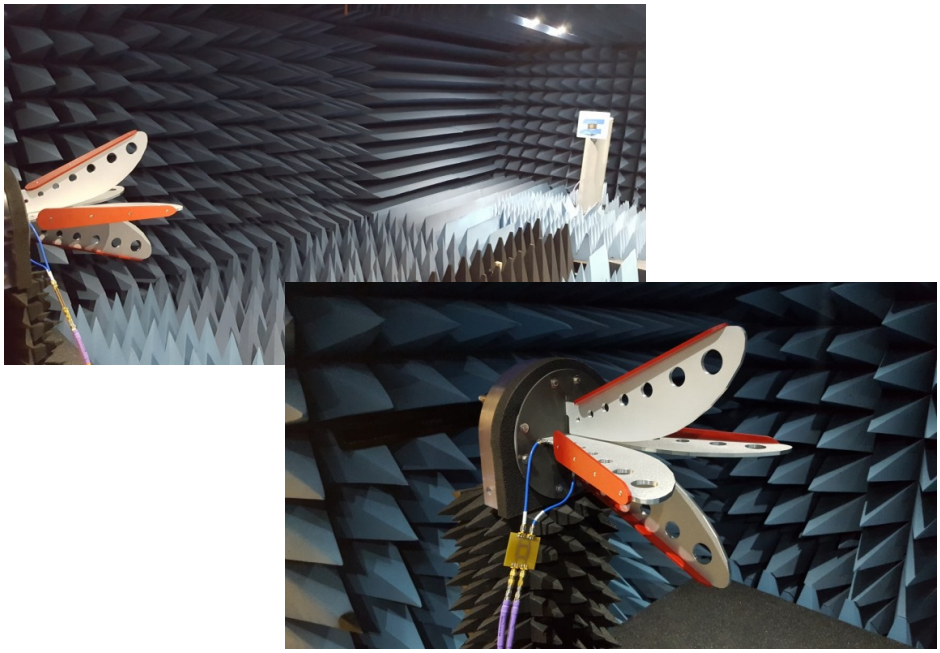

Figure 25: Anechoic Chamber Setup for Radiation Pattern Measurement

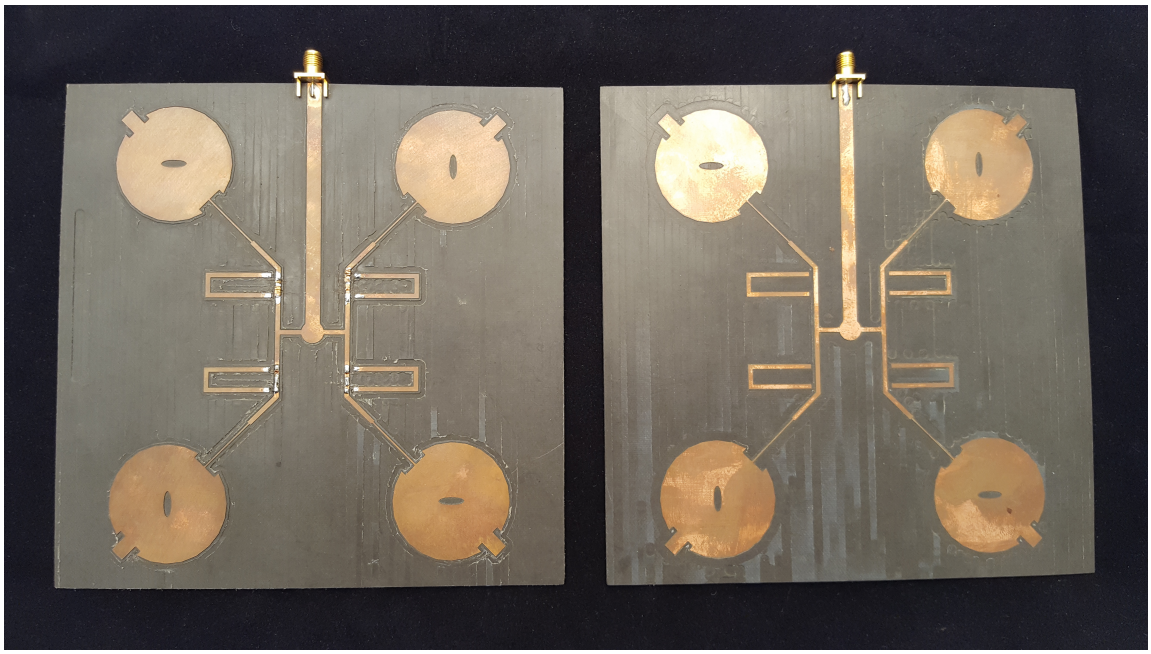

Figure 26: Fabricated Patch Array on Duroid 5880 for Sum Pattern (left) and Difference Pattern (right)

The simulated and measured results are shown below.

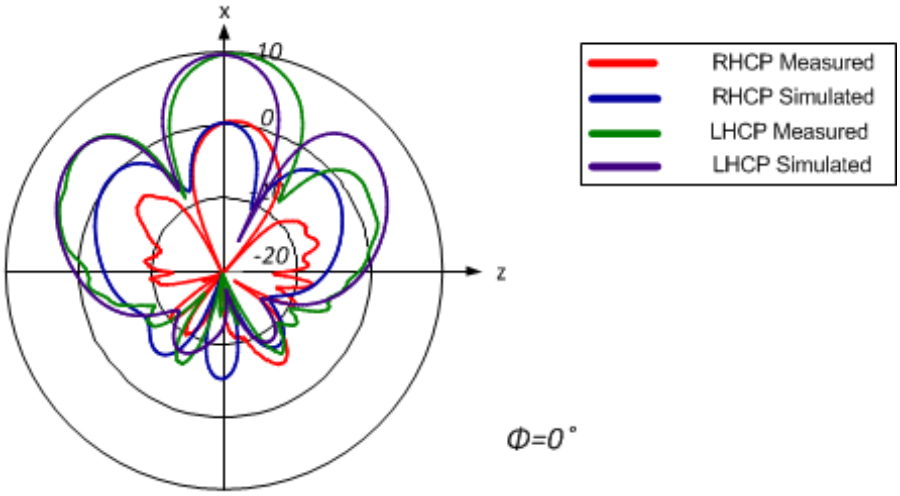

Figure 27: Radiation Pattern for the Sum Configuration

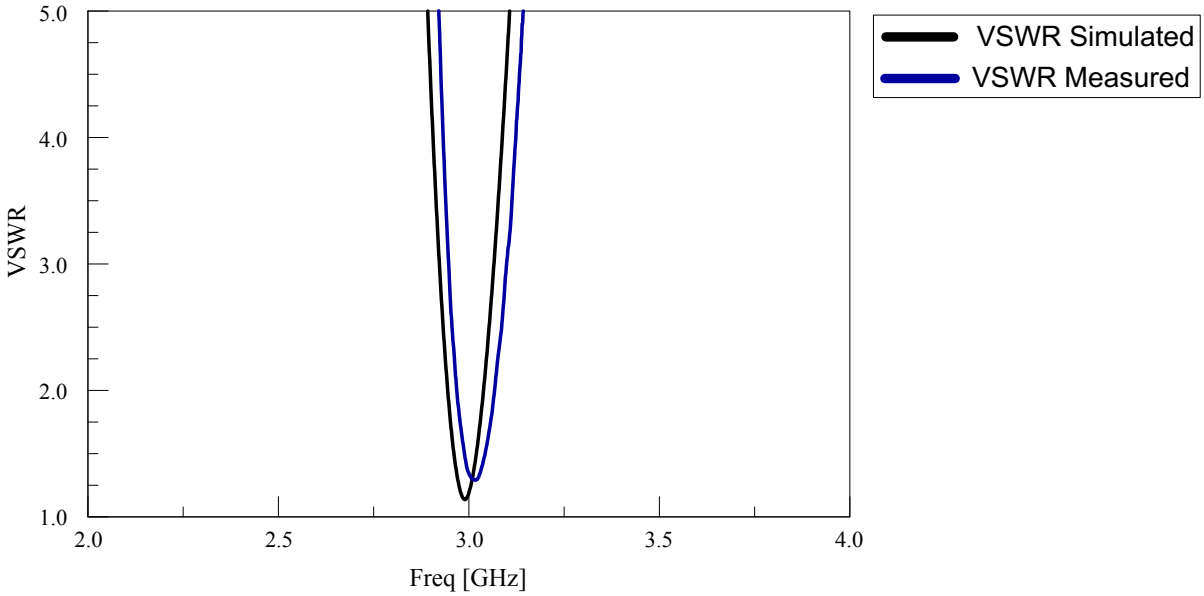

Figure 28: VSWR for the Sum Configuration

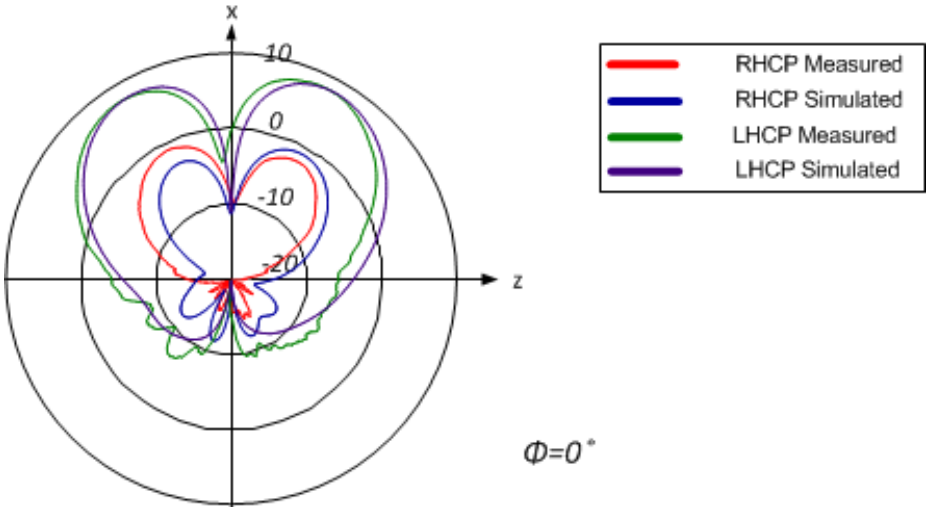

Figure 29: Radiation Pattern for Difference Configuration

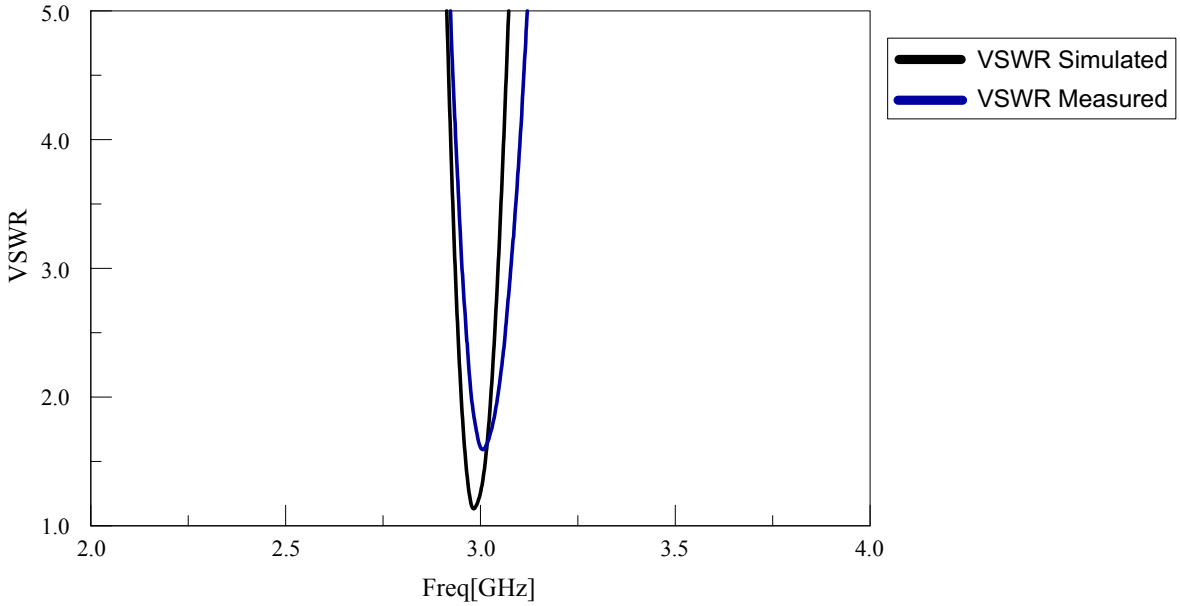

Figure 30: VSWR for Difference Configuration

It is observed that the VSWR for the measured and simulated data for both the configurations are close and approximately equal to 1. This indicates good matching and very less reflected power. The sum configuration has a difference of 12 dB in gain

between the LHCP and the RHCP patterns. The gain of the array is 9.8 dB. Similarly, the difference configuration also has a difference of 12 dB between the LHCP and the RHCP patterns and the gain of the array is 8.4 dB.

5.6. PATCH ARRAY ON MIURA ORI

The patch array in flat configuration is now incorporated into the Miura Ori fold. Both the sum and the difference configurations are simulated in HFSS for different bend angles. The size of the miura ori unit cell is 65 mm × 65 mm and the internal angle of the parallelogram is 80°. The QWT matching for the patch is meandered to address the space considerations.

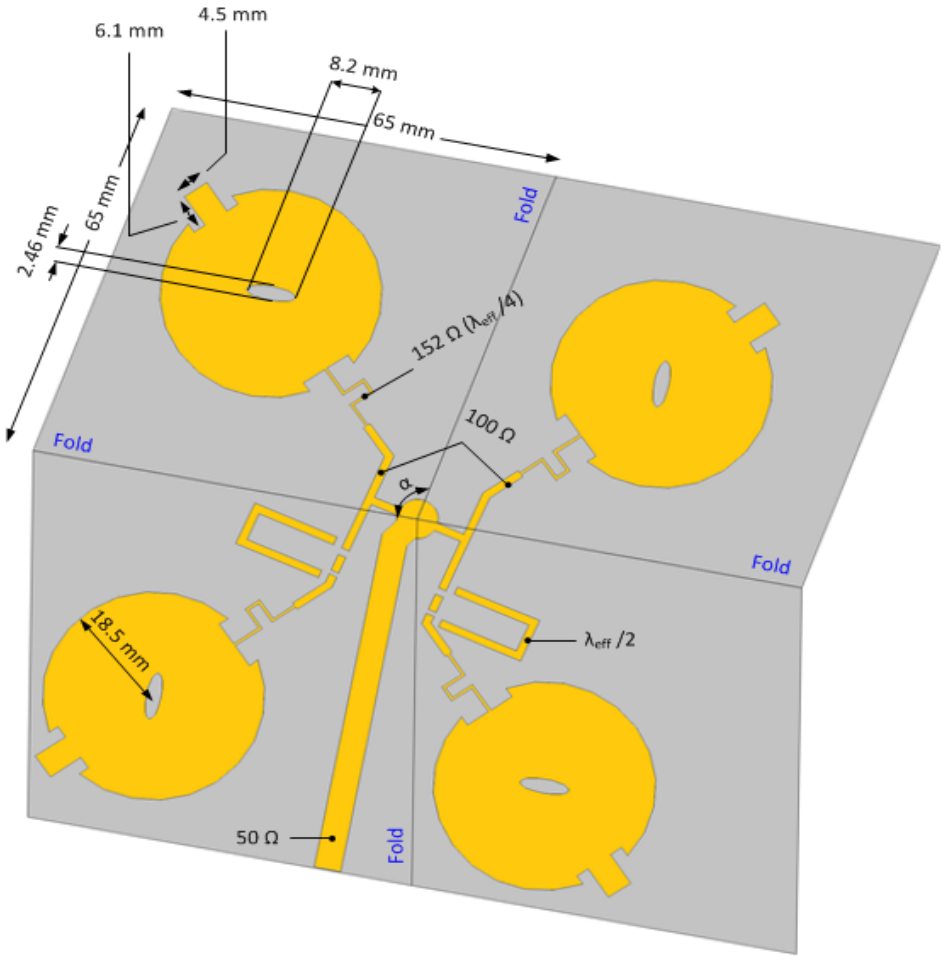

Figure 31: Patch Array on Miura Ori Unit Cell with Sum and Difference Configuration

The simulated results (VSWR and radiation pattern) for 0˚ and 20˚ for the both the configurations are shown below.

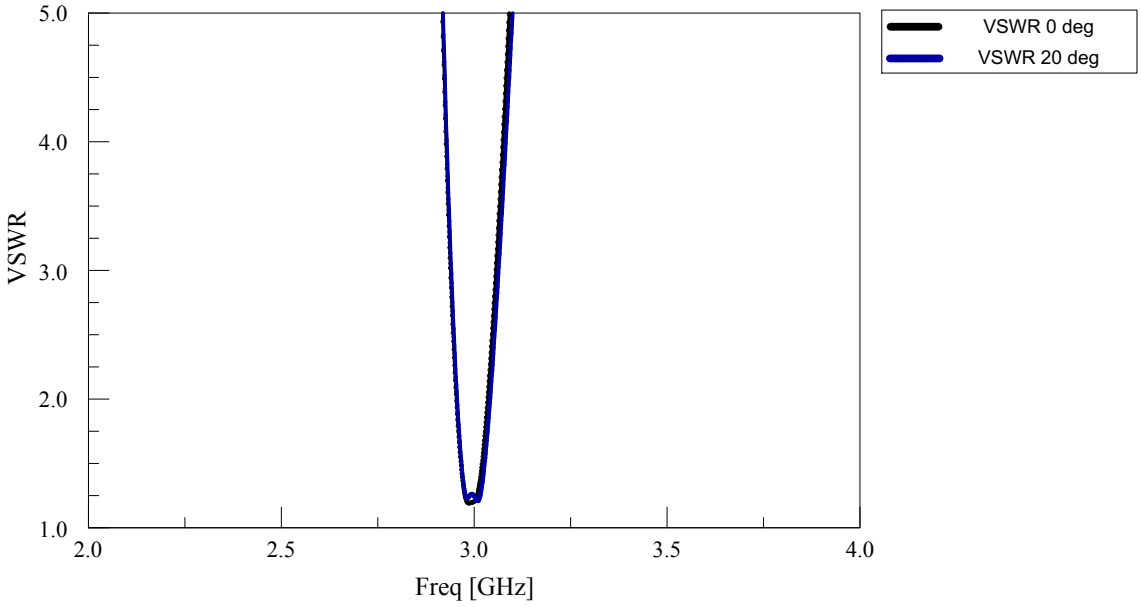

Figure 32: VSWR for Difference Configuration for different bend angles

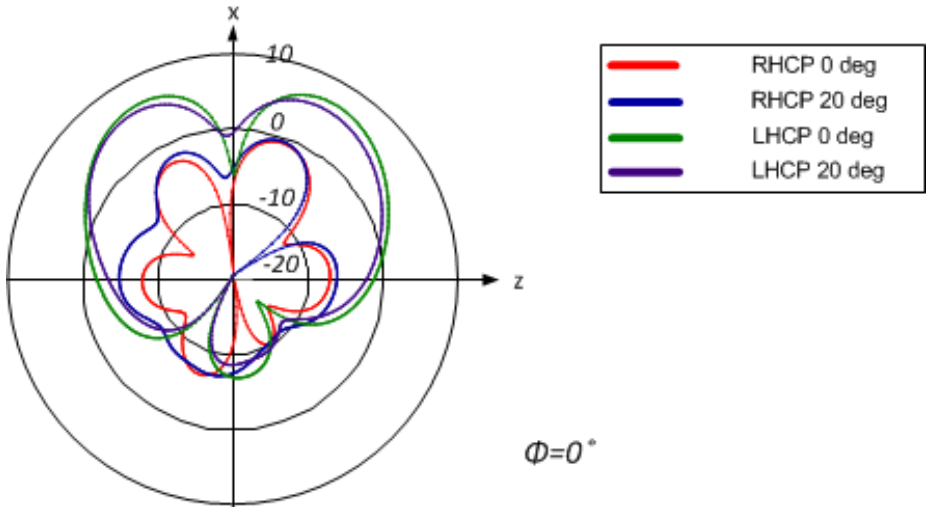

Figure 33: Radiation Pattern for the Difference Configuration for different bend angles

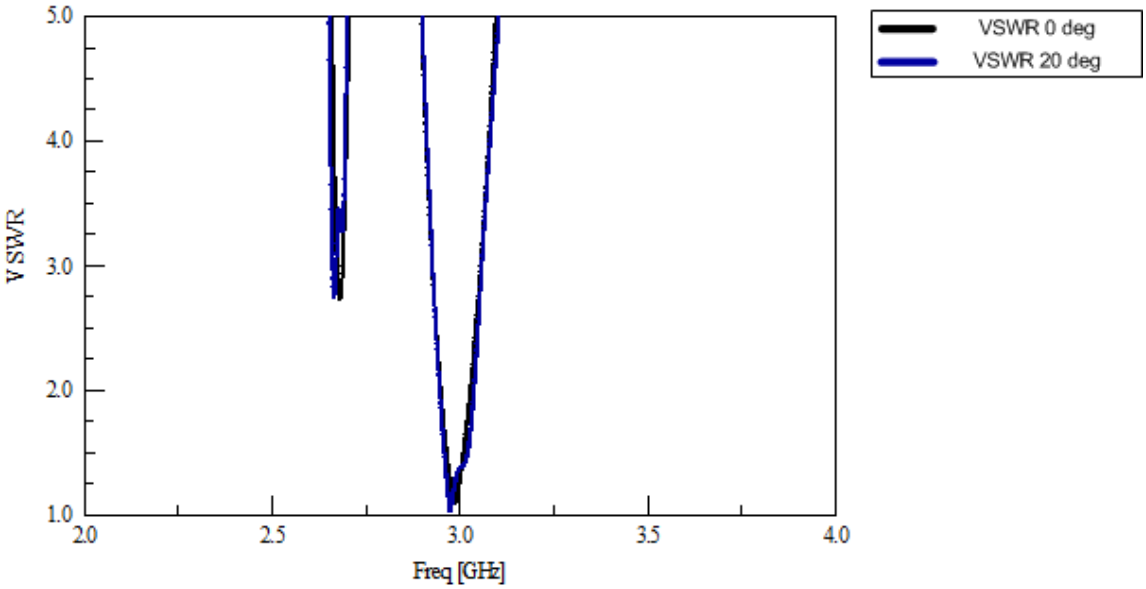

Figure 34: VSWR for Sum Configuration for different bend angles

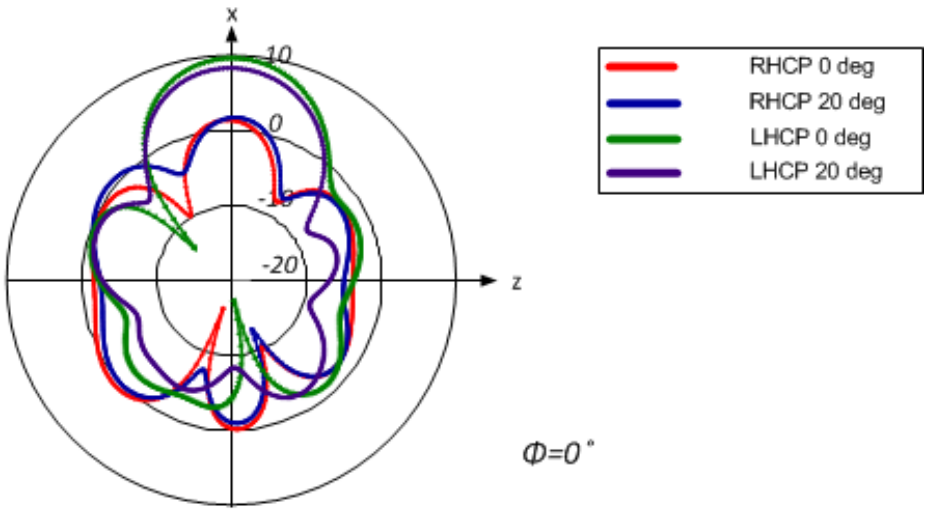

Figure 35: Radiation Pattern for the Sum Configuration for different bend angles

5.7. PATCH ARRAY WITH MODIFIED GROUND PLANE

The removal of ground plane along the folds of the patch solves the folding problem to an extent but the center of the miura unit cell (the apex) is still an issue. Thus, a circular region of radius 1mm is removed in the center of the ground plane. The metal on the top layer i.e. the patch array is still kept as removing that compromises the impedance match of the array. So, a stretchable conductor can be used on the top layer where the metal lies on the miura fold.

This modified array is simulated in HFSS and the flat version is fabricated using a 62 mil RT Duroid 5880 substrate. The simulated and measured results for the radiation pattern and VSWR for the sum and difference configurations are shown. The model is simulated in Ansys HFSS, the measurements for VSWR are taken in Agilent VNA and the radiation pattern is measured using an Anechoic Chamber.

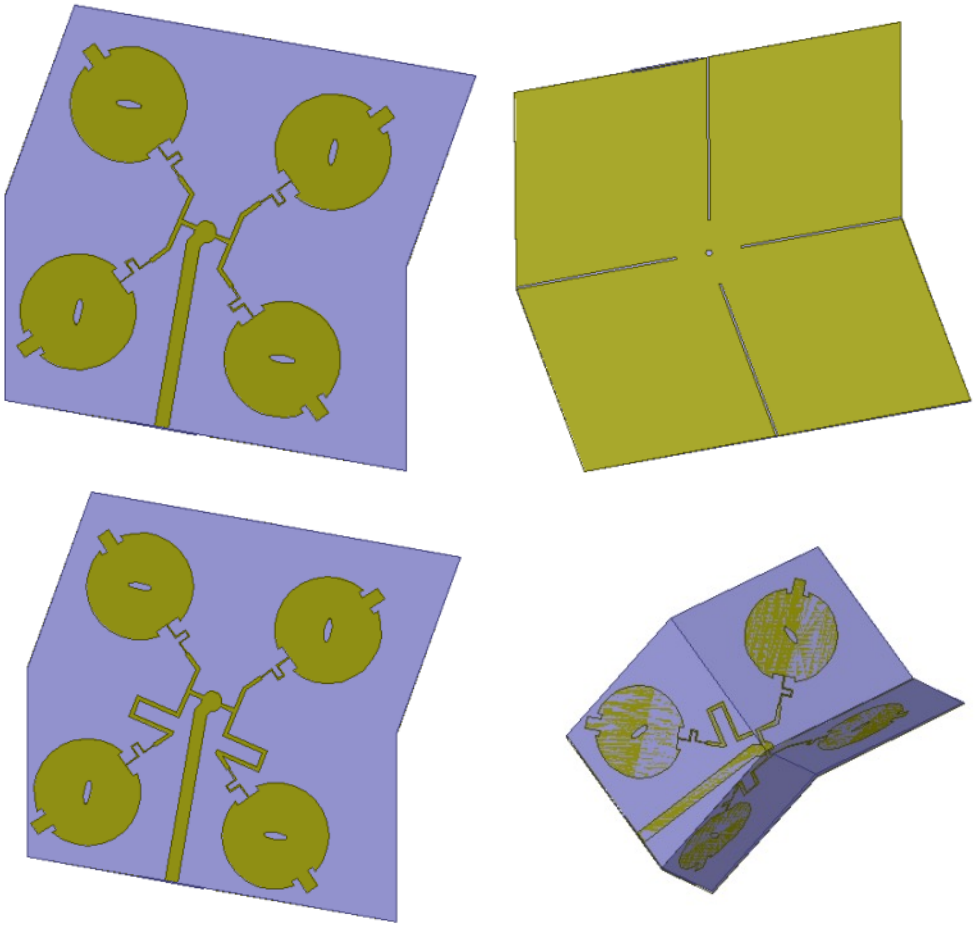

Figure 36: The miura ori array with modified ground plane in the difference, sum and the bent versions

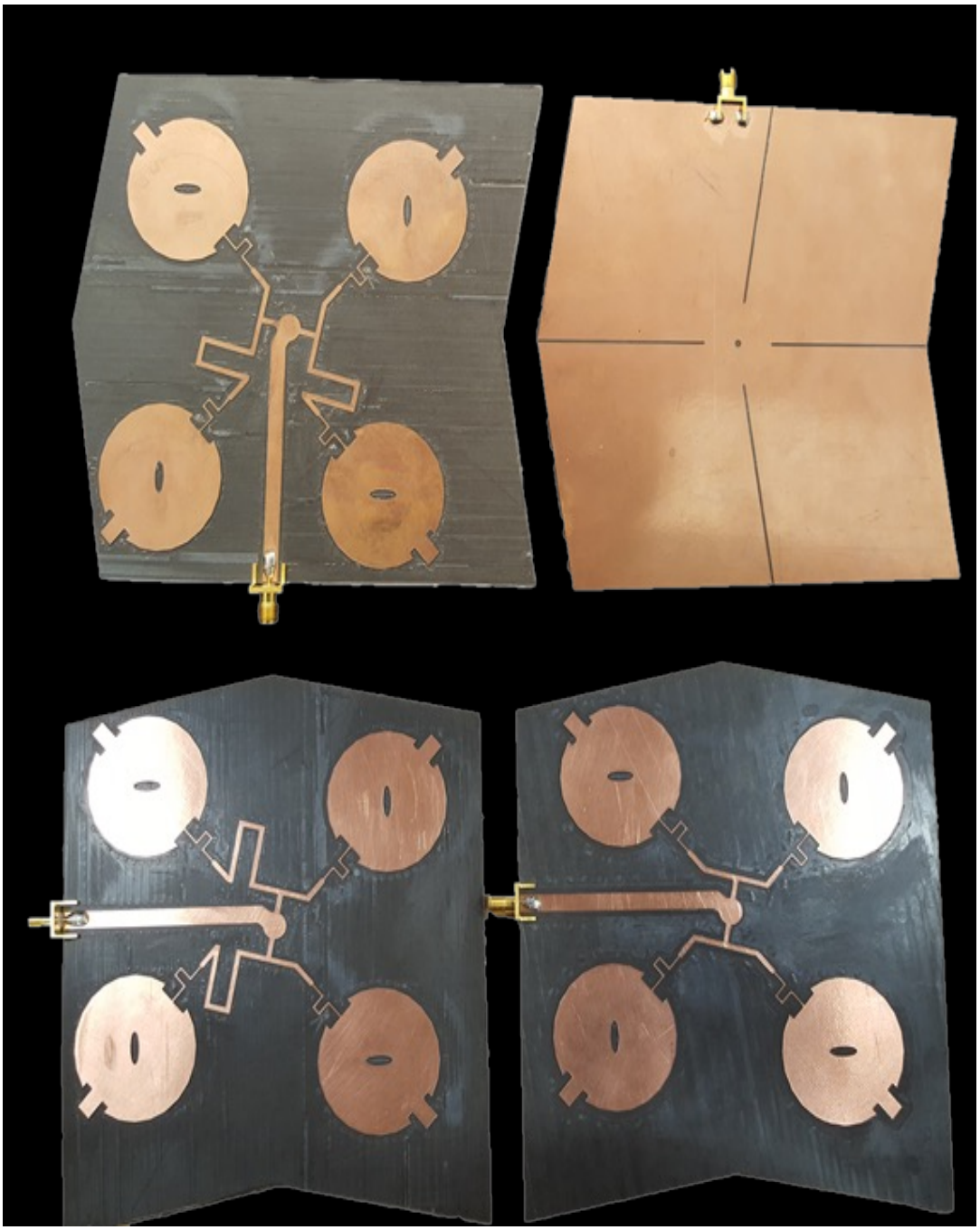

Figure 37: Fabricated Patch Array with modified ground plane

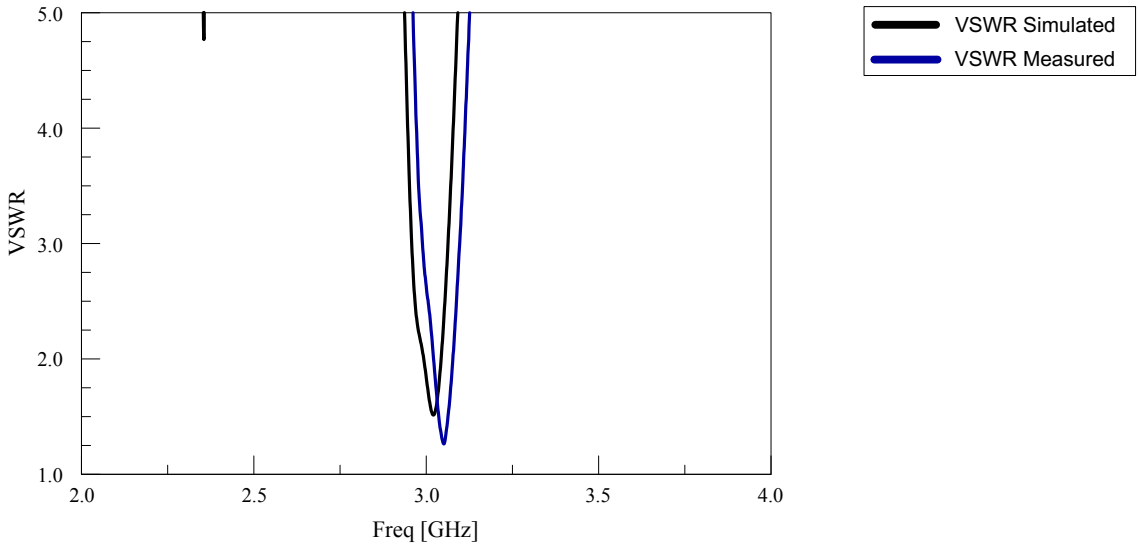

Figure 38: Measured and Simulated VSWR for the 0˚Difference Configuration

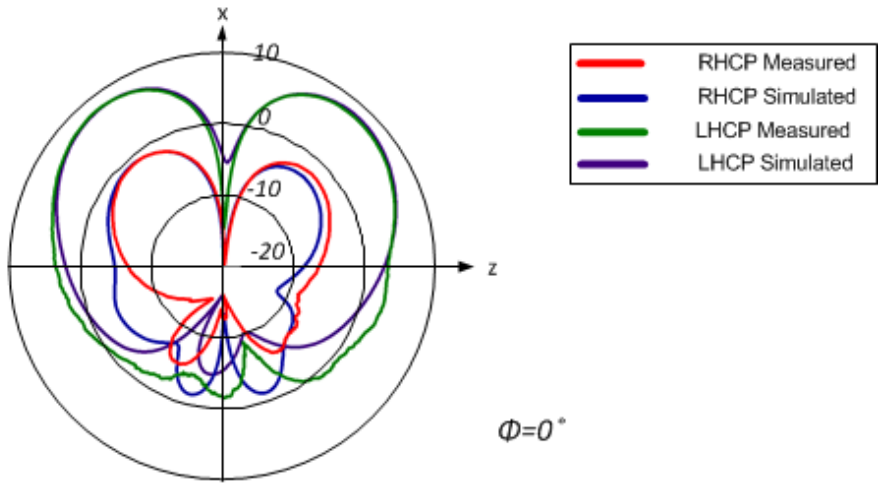

Figure 39: Measured and Simulated Radiation Pattern for the 0˚Difference Configuration

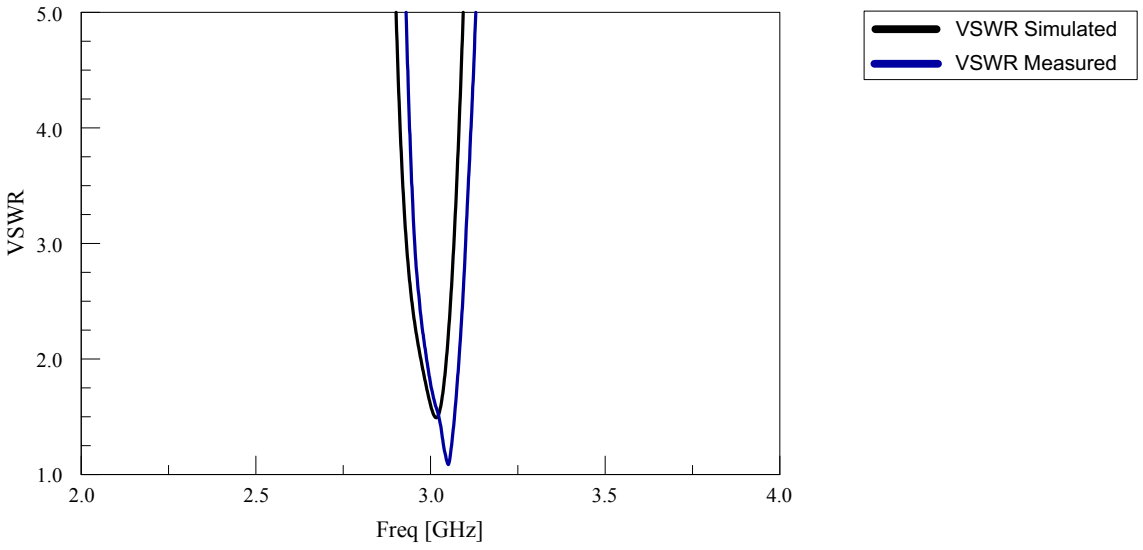

Figure 40: Measured and Simulated VSWR for the 0˚Sum Configuration

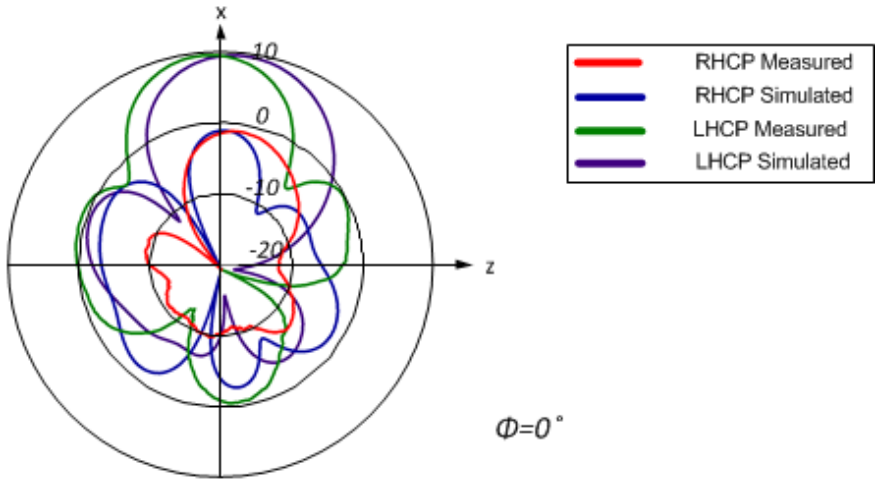

Figure 41: Measured and Simulated Radiation Pattern for the 0˚Sum Configuration

6. ARRAY FACTOR AND IMPACT OF FOLDING

6.1. ARRAY FACTOR

The array factor of a uniform planar array is given by (2.35). The distance between the array elements of the unit cell changes as the array is folded. Initially, the center to center distance between two elements along x- and y- directions is taken as 62 mm. The wavelength of light in Duroid is 73 mm. As the array folds, the distance between the elements changes according to the following formulae.

$$S = b\frac{\cos\theta\tan\gamma}{\sqrt{1+\cos^2\theta\tan^2\gamma}} \tag{5.1}$$

$$L = a\sqrt{1-\sin^2\theta\sin^2\gamma} \tag{5.2}$$

Where S and L are the lengths along x and y axes respectively. The angle γ is the angle between adjacent sides of the parallelogram. The angle θ is the bend angle of the fold. Thus, in the design $\gamma = 80^{\circ}$ and θ varies depending on the degree of the fold. The spacing of the array is uniform along both x and y directions and is equal to 62 mm. Therefore, $a = 62\ mm$ and $b = 62\ mm$. Using equations (5.1) and (5.2), the calculated S and L are tabulated below. Thus, as the array is folded more, the array factor shrinks and the gain reduces.

θ (deg)	S (mm)	L (mm)
0	62	62
10	61	61.1
20	60.9	58.4
30	60.8	54
40	60.4	48
50	59.8	40.7
60	58.5	32.4

Table 4: Calculated spacing between array elements as the array is folded

6.2. ARRAY FACTOR IN HFSS

The single circular patch element is considered and using the antenna array setup in HFSS, the array factor is created for different bend angles. It is observed that as the spacing between the elements reduces, the array factor shrinks i.e. the side lobes decreases and the beamwidth increases. This is illustrated by the following plots. A 10×10 array is considered for the analysis.

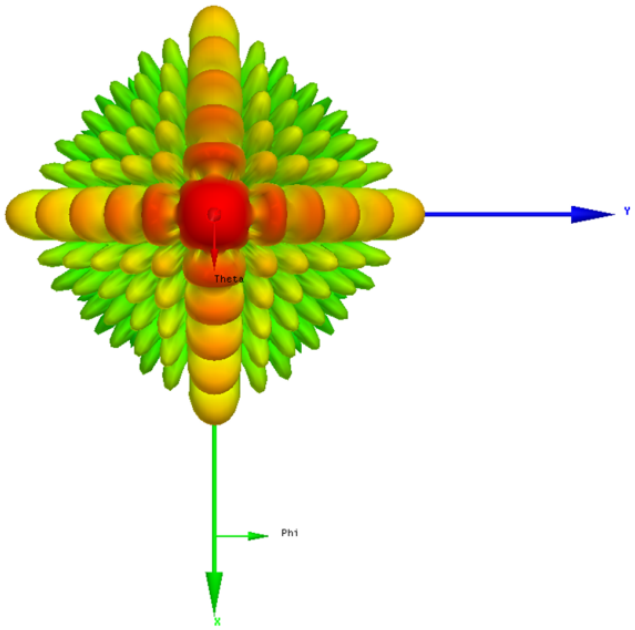

Figure 42: 3D Pattern of Array factor for 0˚

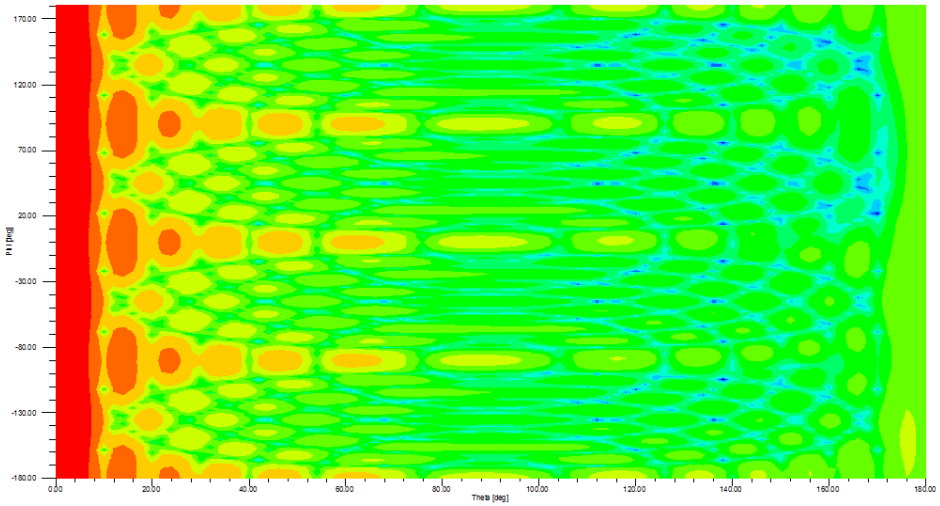

Figure 43: Contour Plot of Array factor for 0˚

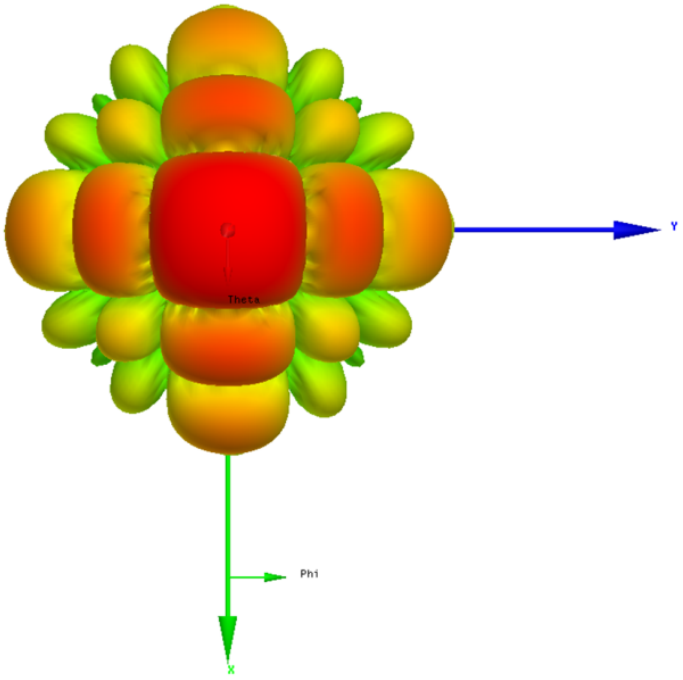

Figure 44: 3D Pattern of Array factor for 60˚

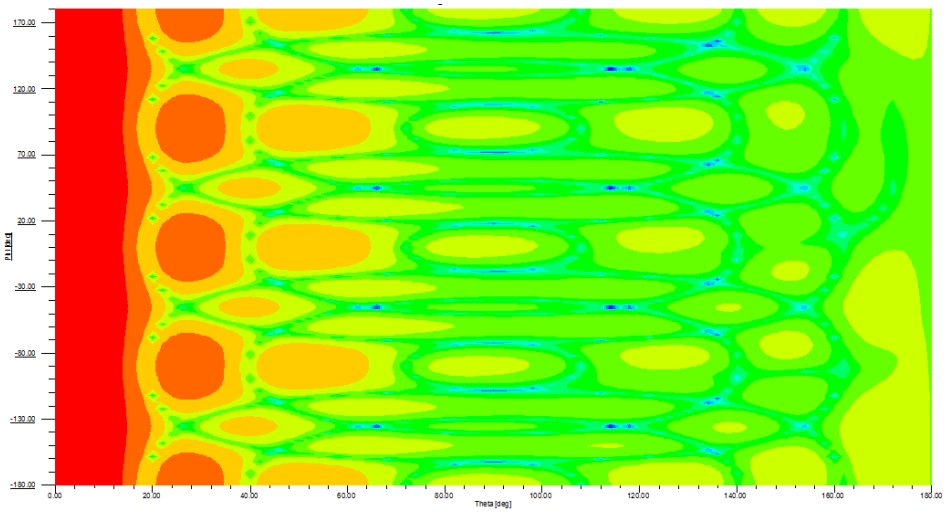

Figure 45: Contour Plot of Array factor for 60˚

6.3. IMPEDANCE AND RADIATION BEHAVIOR

A parametric analysis is performed to study the impact of folding the patch array inwards and outwards. It is observed that due to the increase in coupling between the adjacent elements and the shielding of the ground plane during the bending process, the gain of the array decreases and the beamwidth increases as the bend angle increases. Also, the impedance match of the array becomes poor.

The difference in gain between the LHCP and the RHCP also decreases i.e. the circular polarization property gradually decreases. The shape of the pattern also changes as a result. Folding the array outward is better than folding the array inward as folding inward results in additional shielding due to the ground plane. This is illustrated for both sum and difference configurations for various bend angles for both inward and outward folding. The simulations are performed in HFSS.

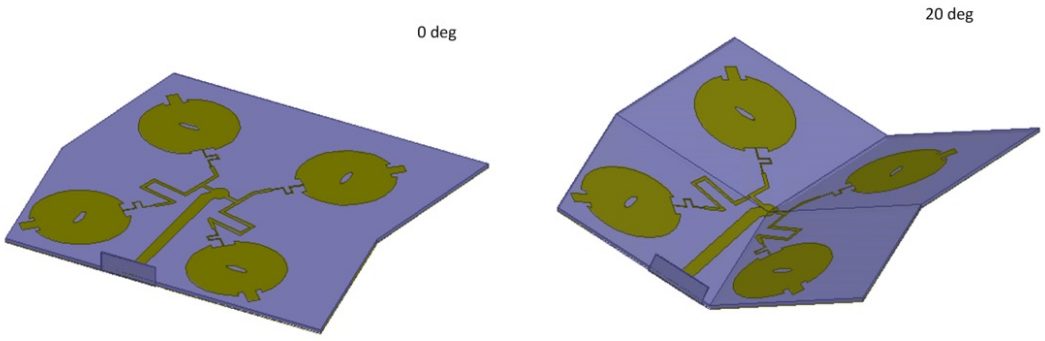

Figure 46: Patch Array folding inward

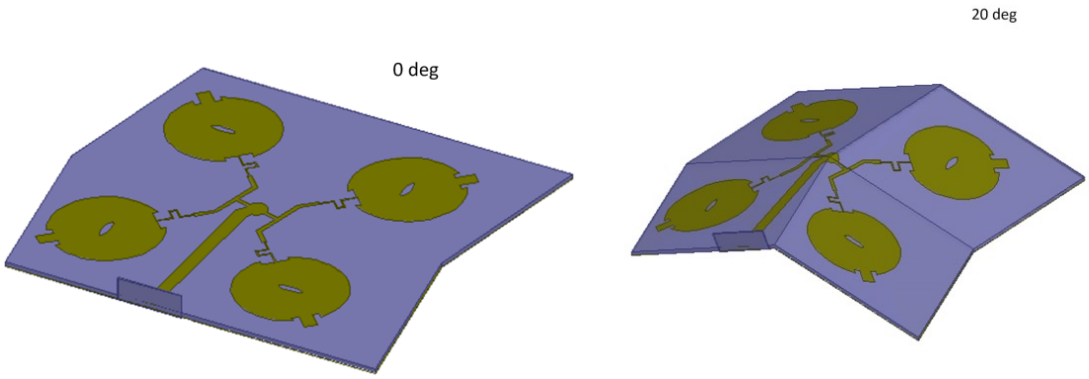

Figure 47: Patch Array folding outward

The changes in the impedance match and radiation behavior as the patch array in difference configuration folds inward and outward is shown below.

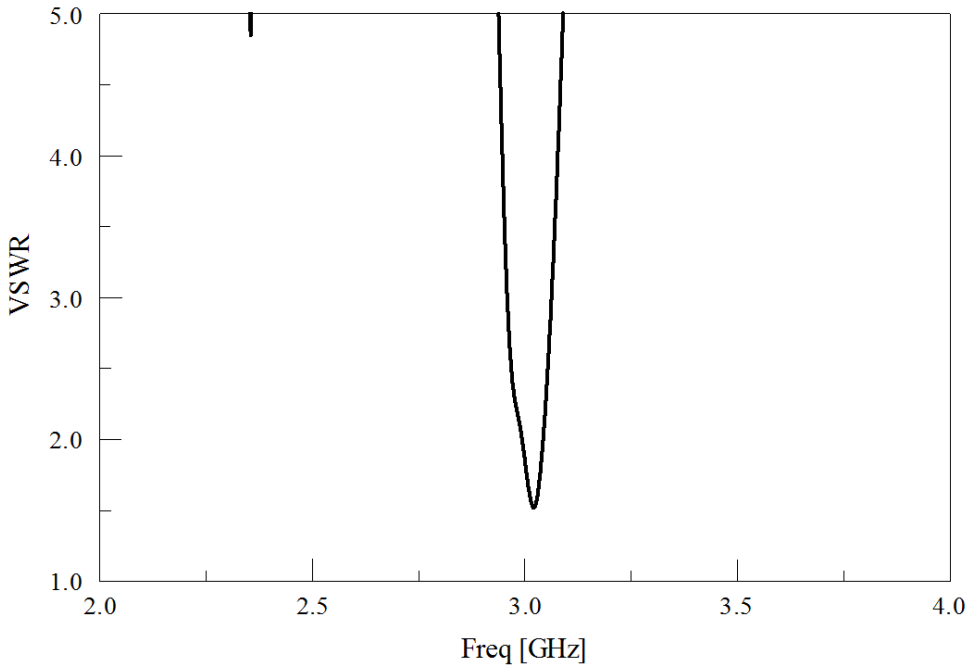

Figure 48: VSWR for Difference Configuration 0˚

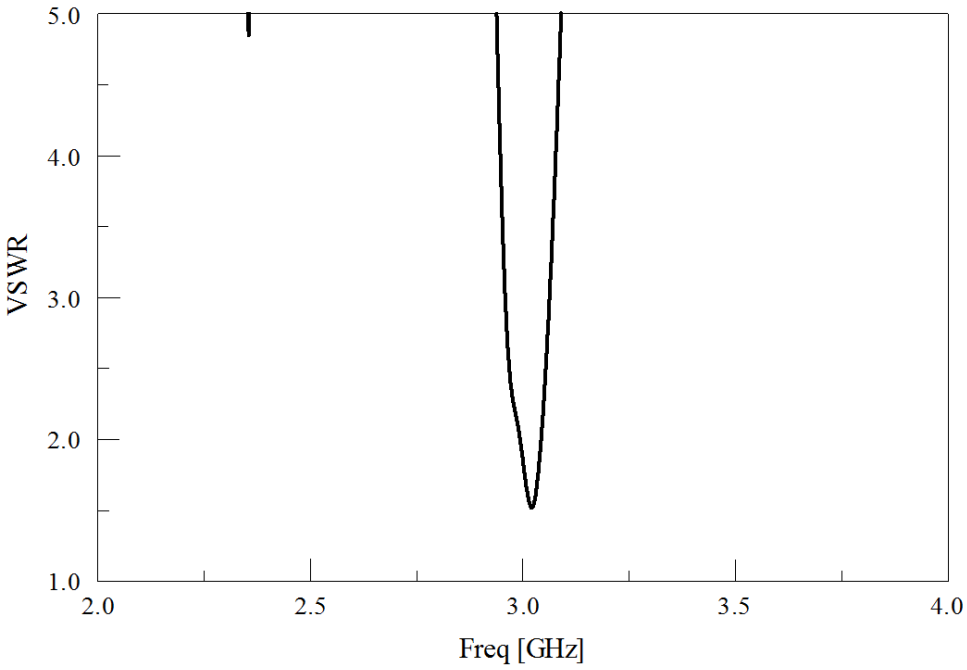

Figure 49: VSWR for Difference Configuration folding inward 20˚

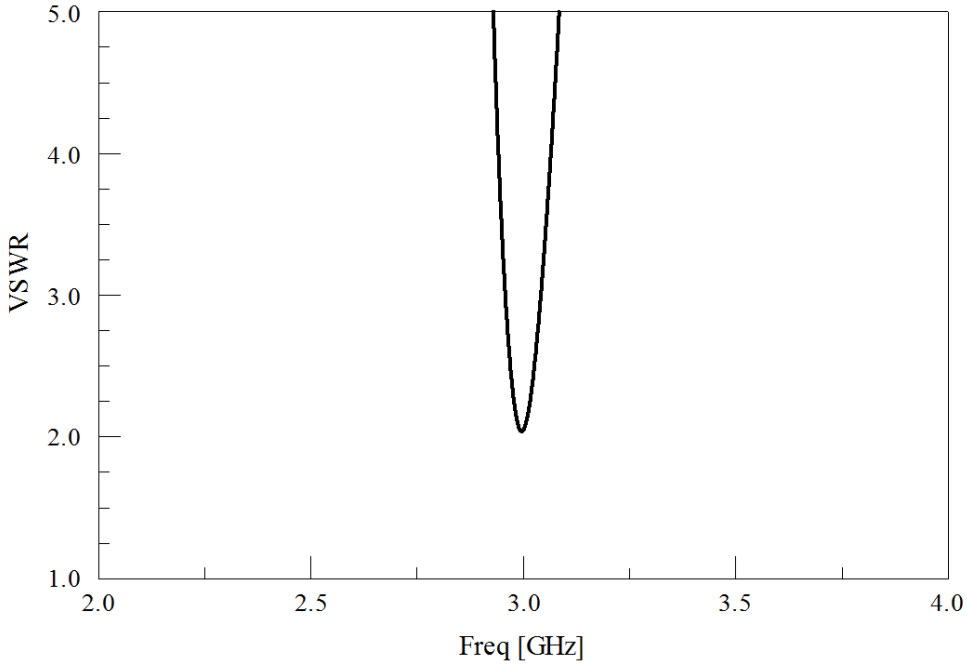

Figure 50: VSWR for Difference Configuration folding inward 40˚

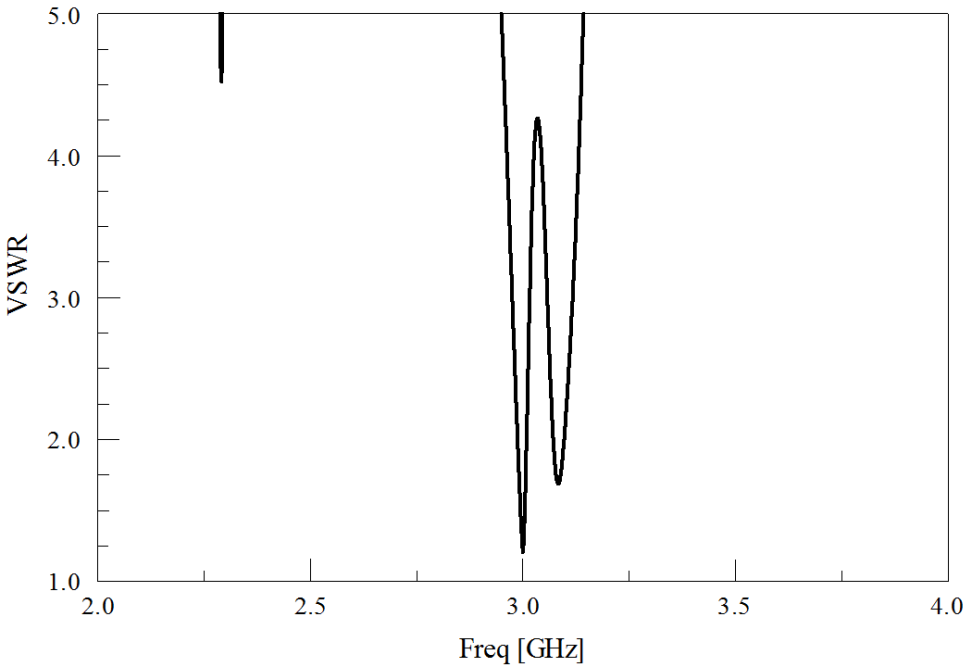

Figure 51: VSWR for Difference Configuration folding inward 60˚

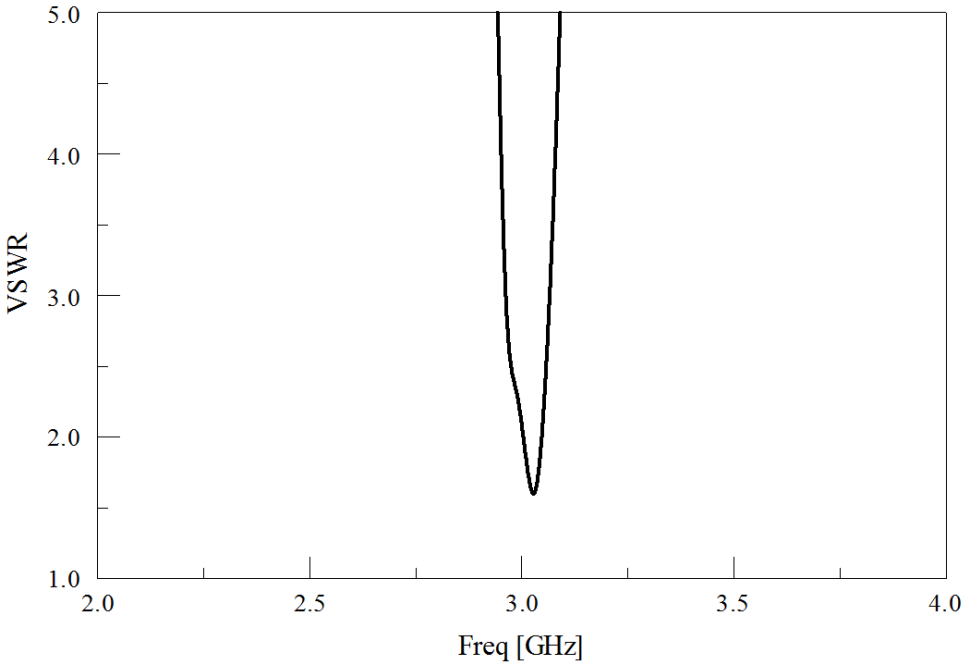

Figure 52: VSWR for Difference Configuration folding outward 20˚

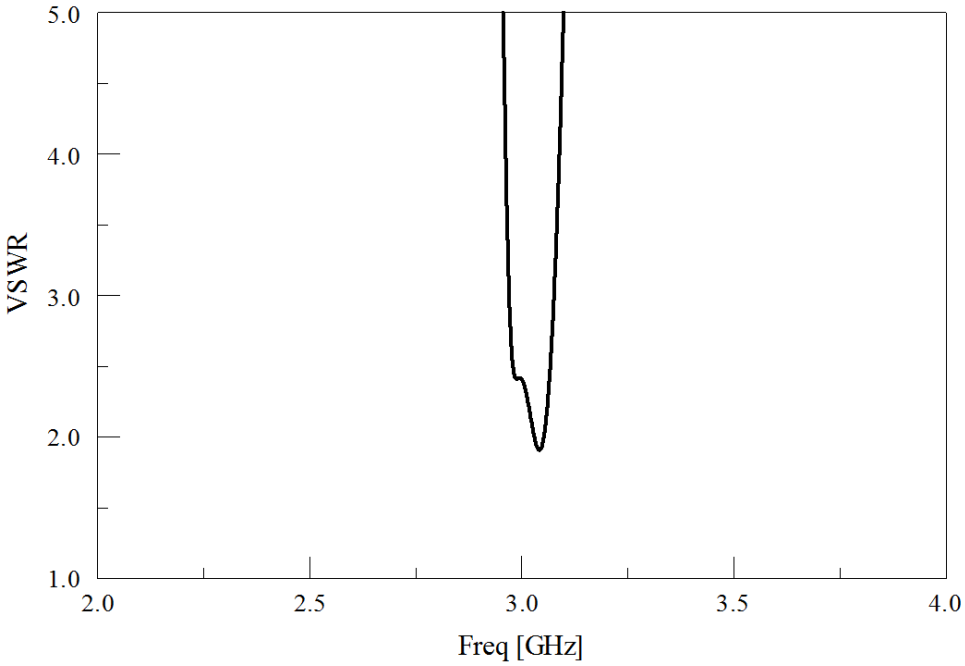

Figure 53: VSWR for Difference Configuration folding outward 40˚

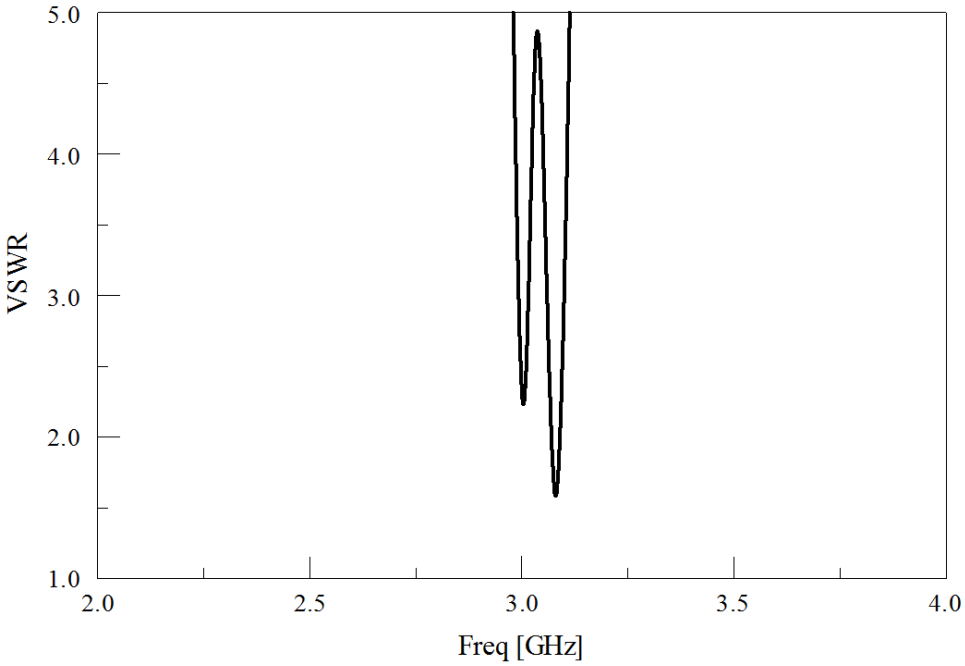

Figure 54: VSWR for Difference Configuration folding outward 60˚

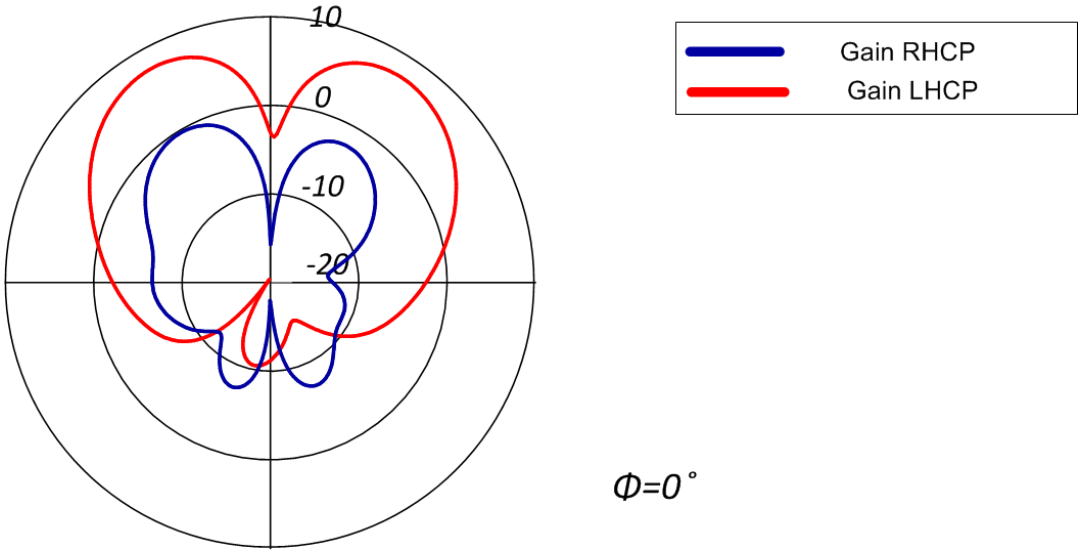

Figure 55: Radiation Pattern for Difference Configuration 0˚

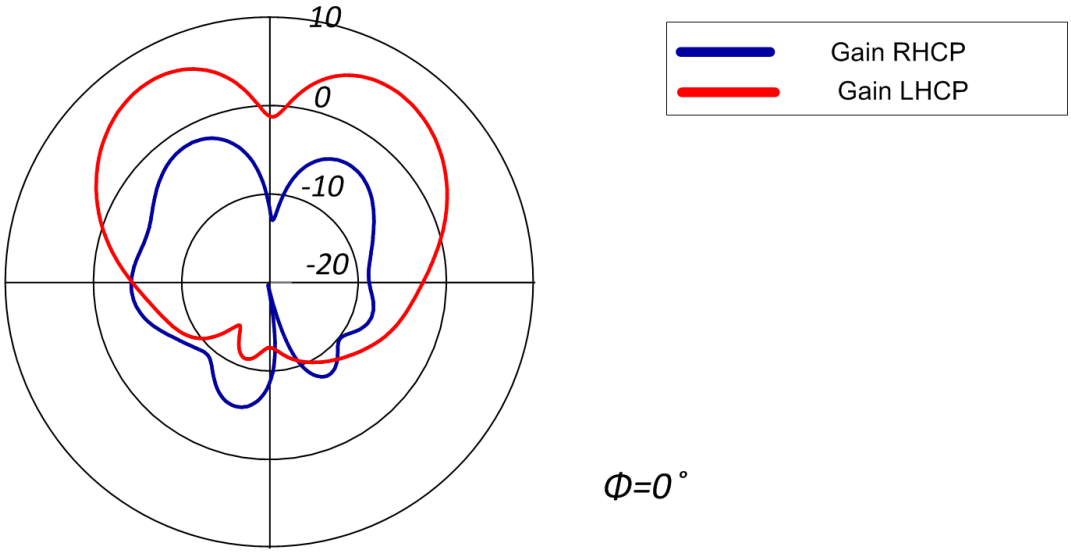

Figure 56: Radiation Pattern for Difference Configuration folding inward 20˚

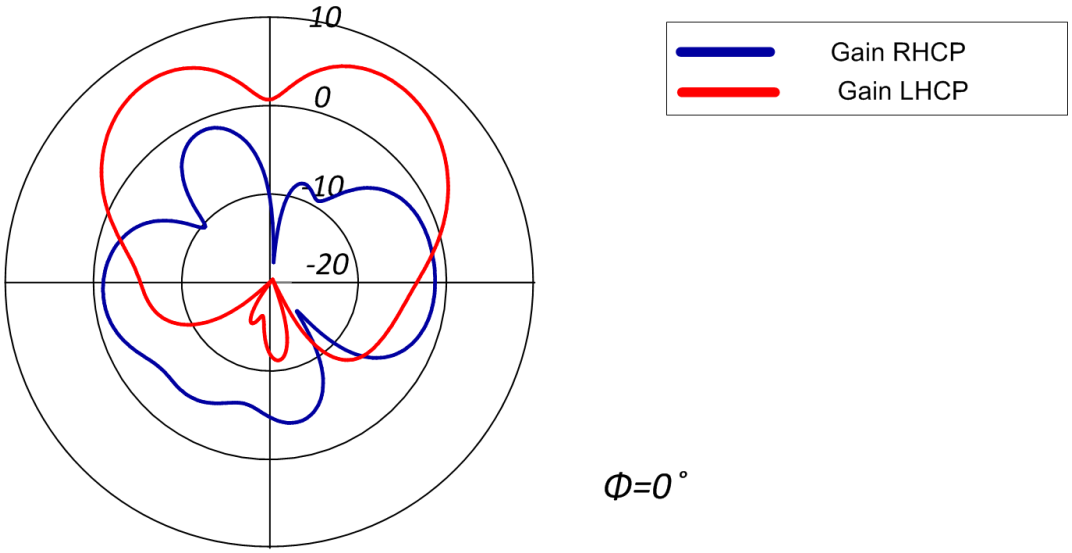

Figure 57: Radiation Pattern for Difference Configuration folding inward 40˚

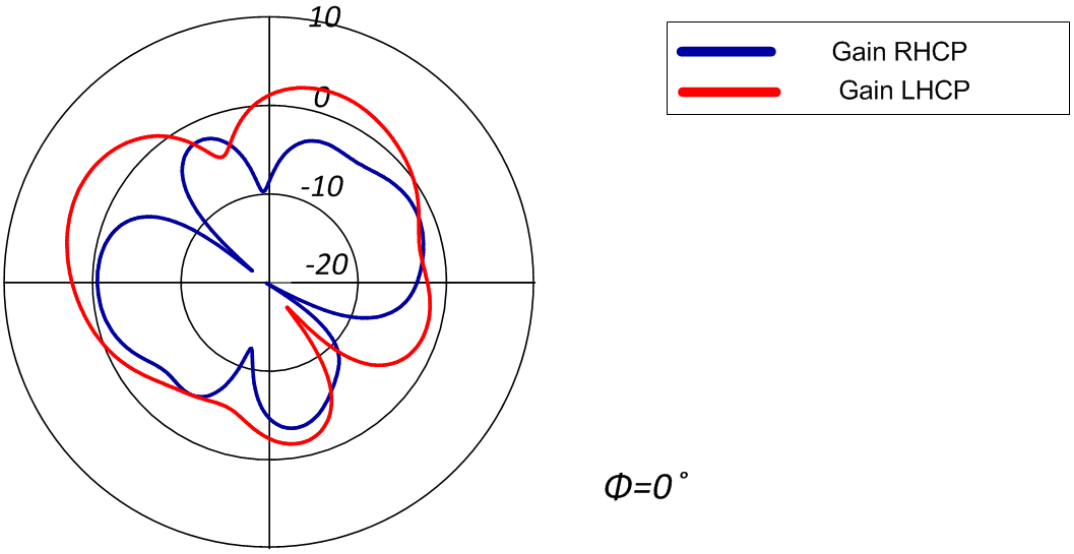

Figure 58: Radiation Pattern for Difference Configuration folding inward 60˚

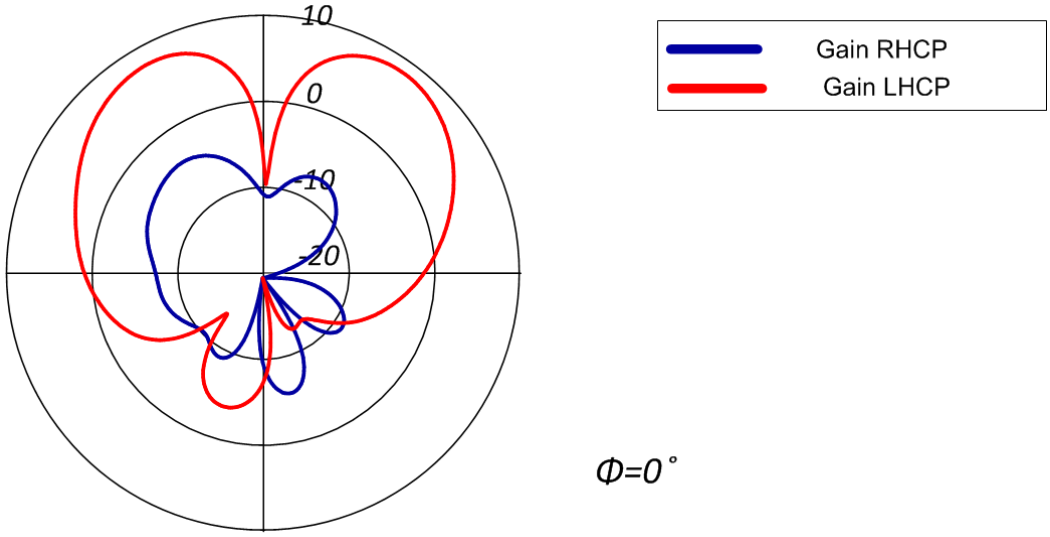

Figure 59: Radiation Pattern for Difference Configuration folding outward 20˚

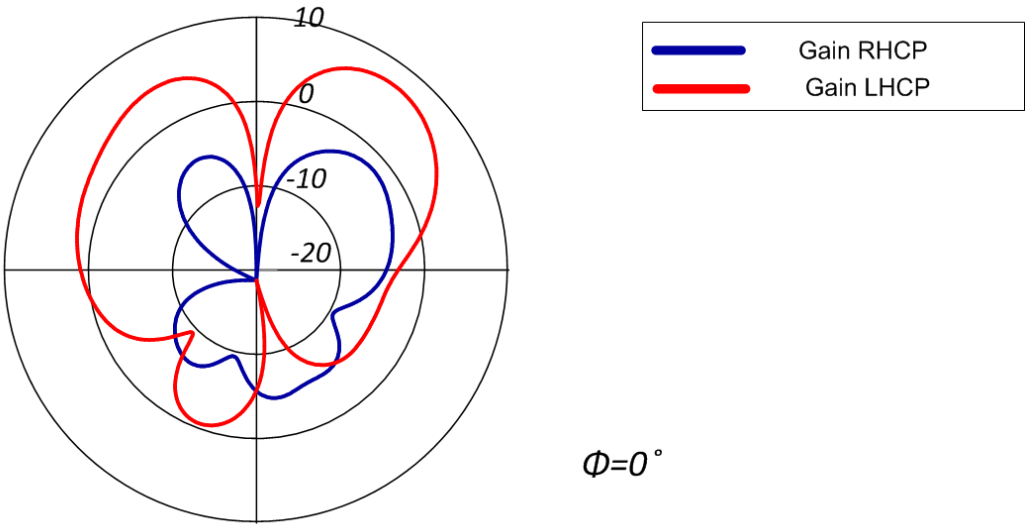

Figure 60: Radiation Pattern for Difference Configuration folding outward 40˚

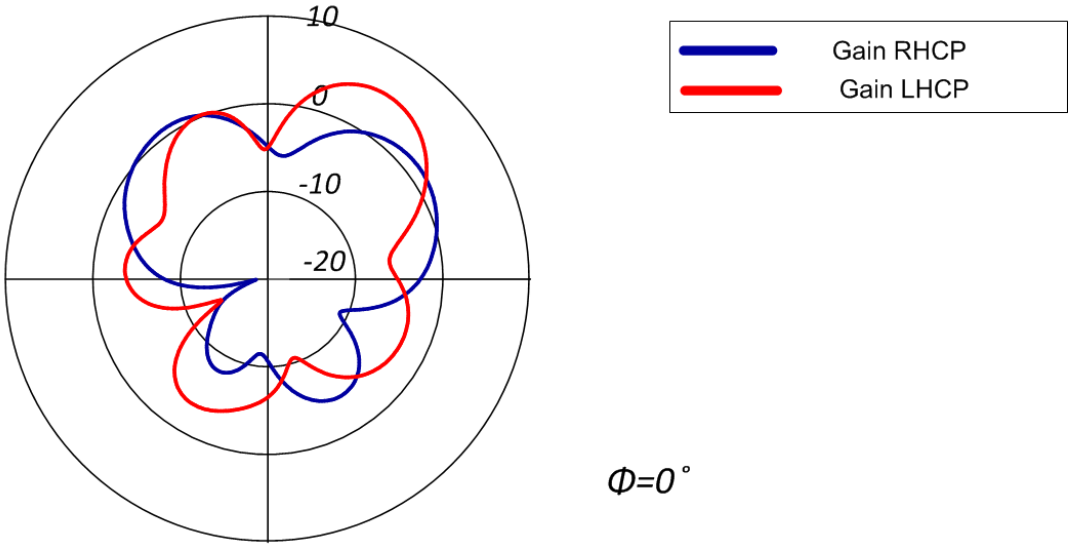

Figure 61: Radiation Pattern for Difference Configuration folding outward 60°

The changes in the impedance match and radiation behavior as the patch array in sum configuration folds inward and outward is shown below.

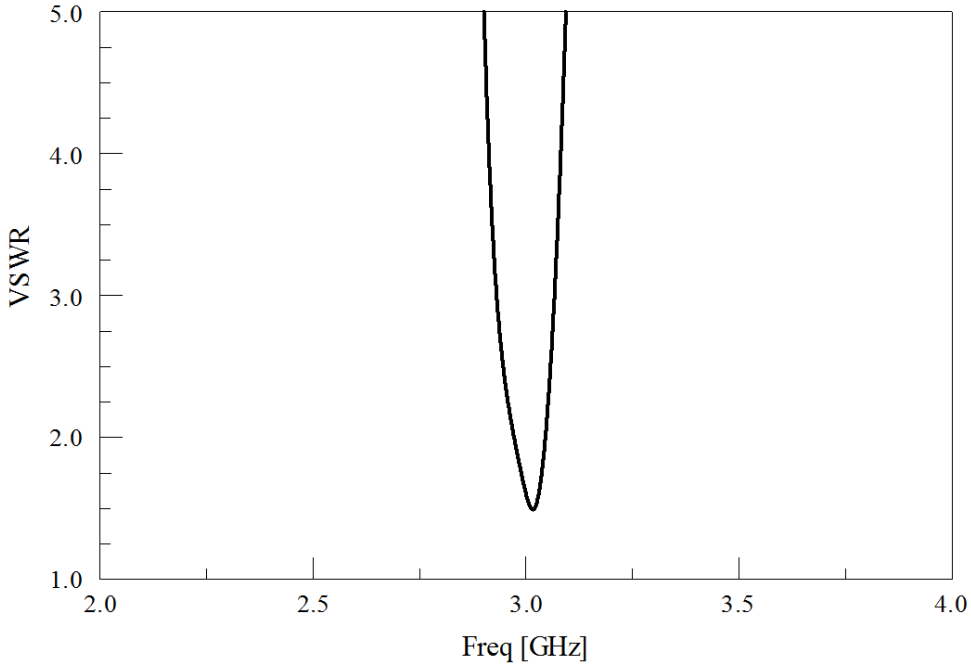

Figure 62: VSWR for Sum Configuration 0°

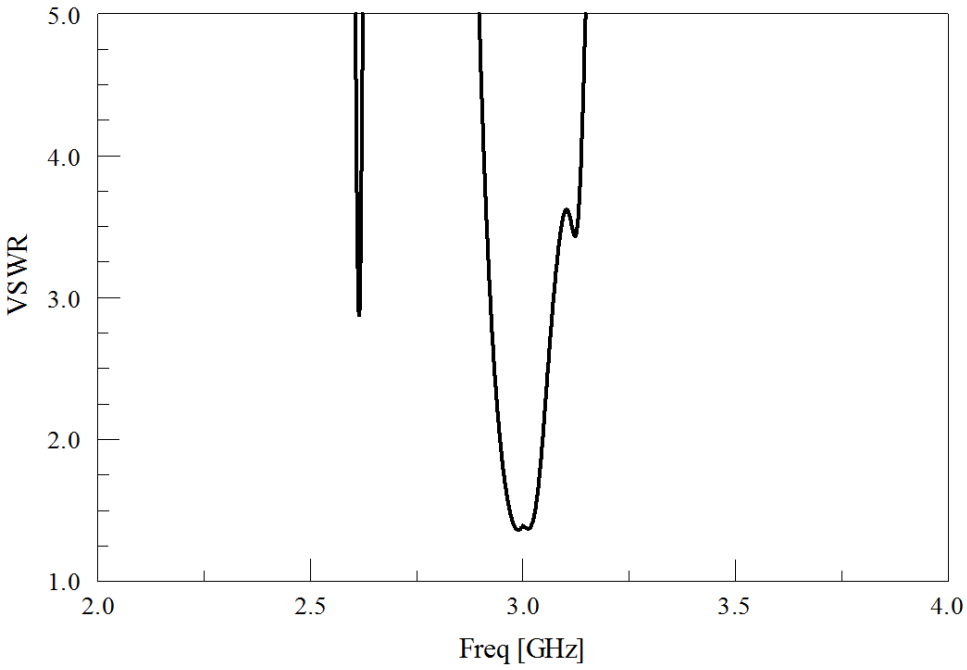

Figure 63: VSWR for Sum Configuration folding inward 20˚

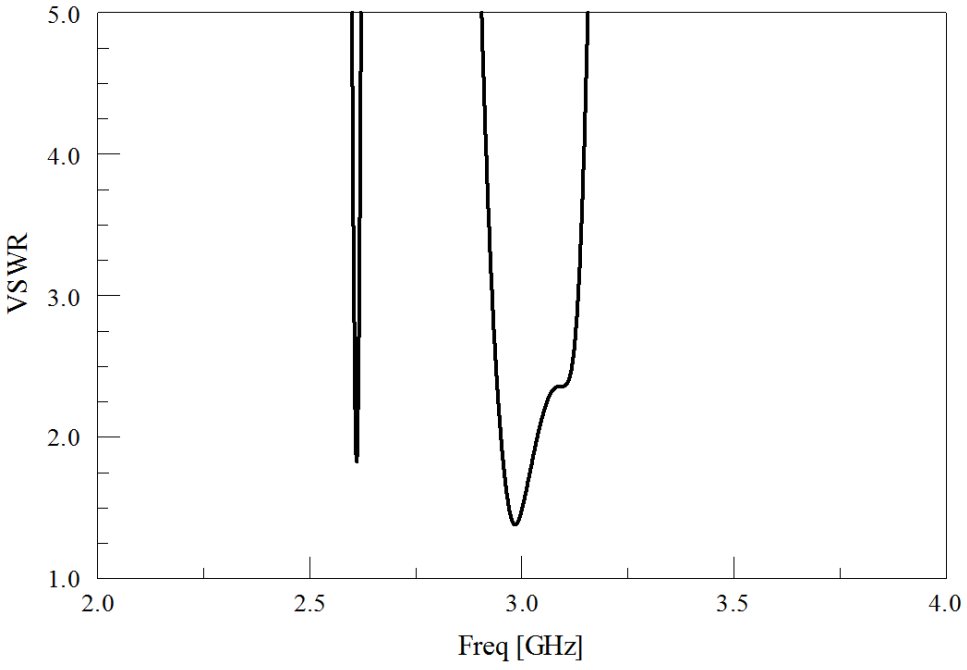

Figure 64: VSWR for Sum Configuration folding inward 40˚

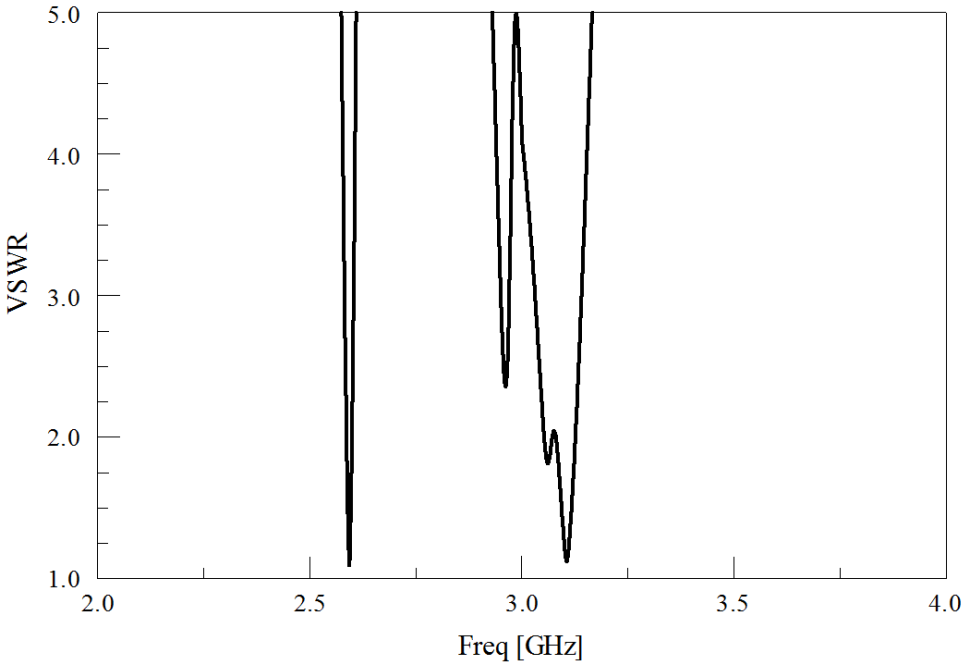

Figure 65: VSWR for Sum Configuration folding inward 60˚

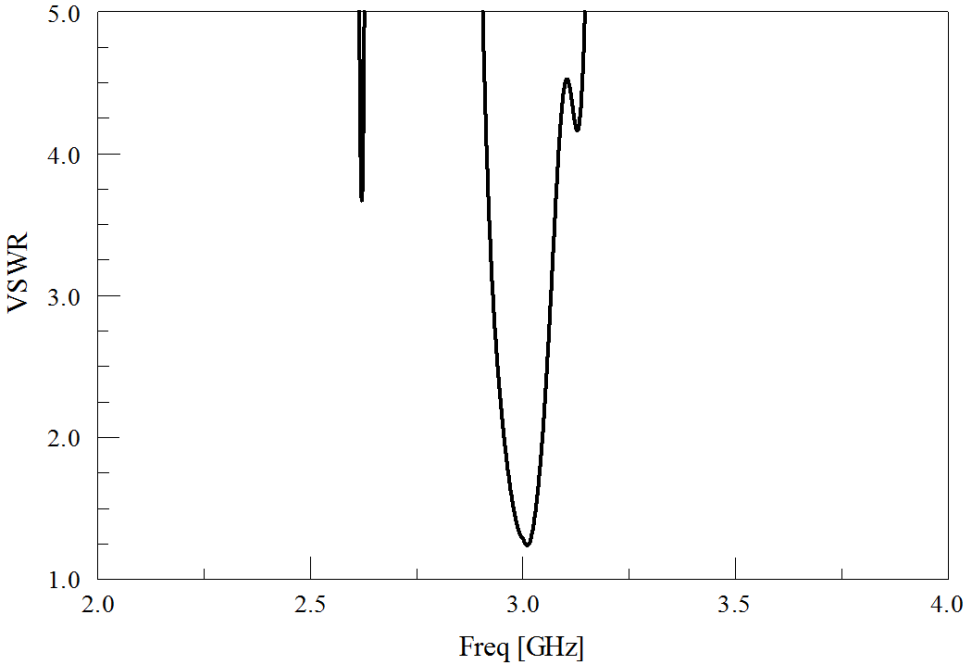

Figure 66: VSWR for Sum Configuration folding outward 20˚

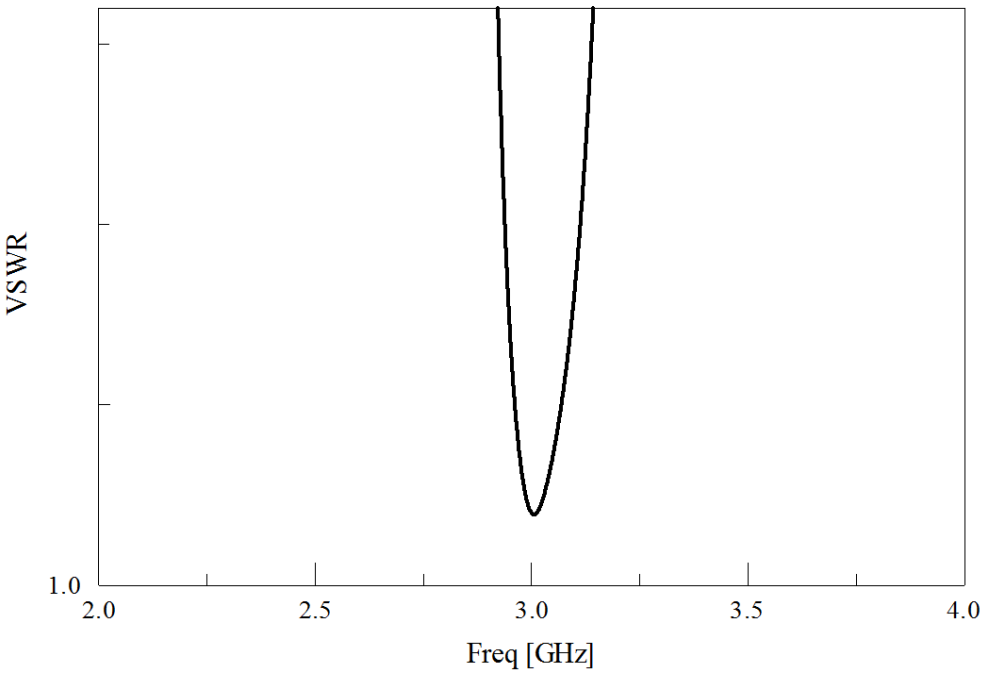

Figure 67: VSWR for Sum Configuration folding outward 40˚

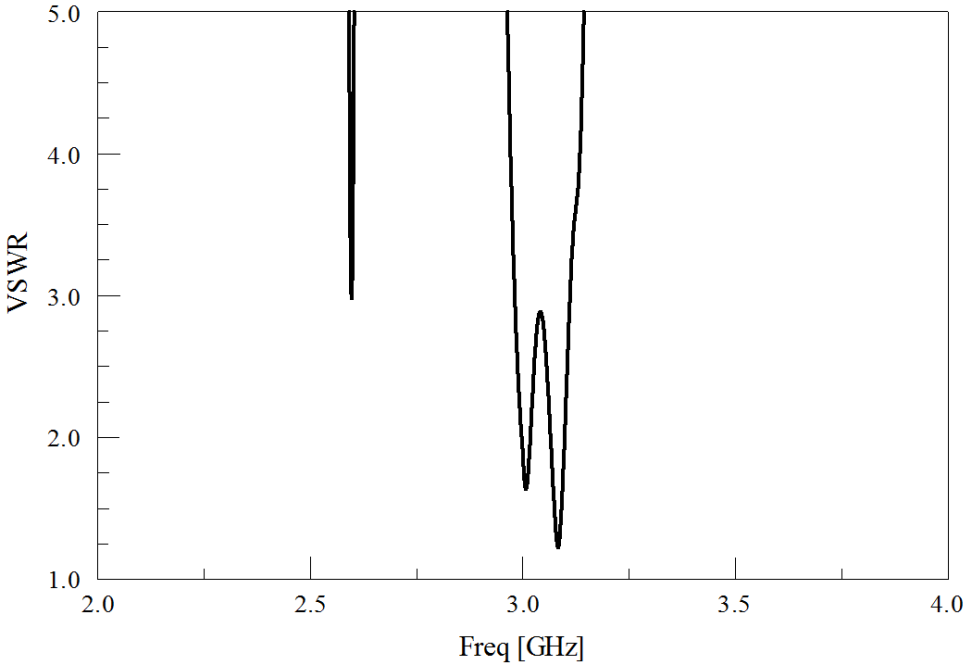

Figure 68: VSWR for Sum Configuration folding outward 60˚

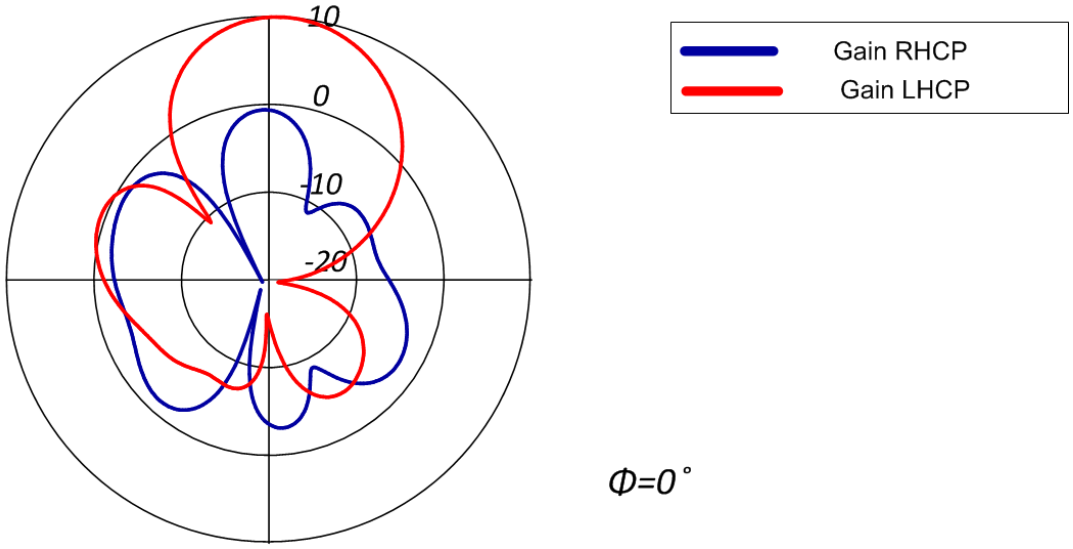

Figure 69: Radiation Pattern for Sum Configuration 0˚

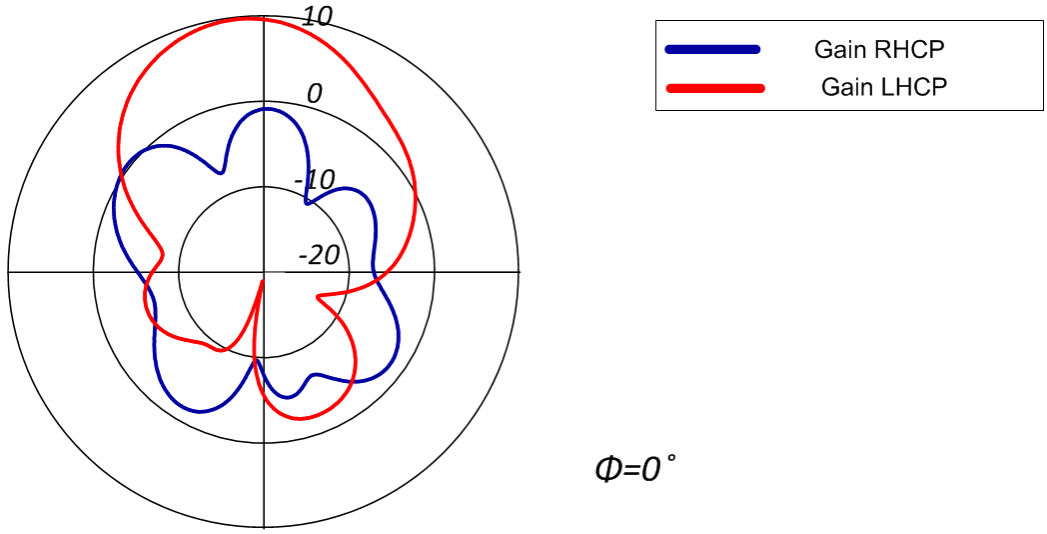

Figure 70: Radiation Pattern for Sum Configuration folding inward 20˚

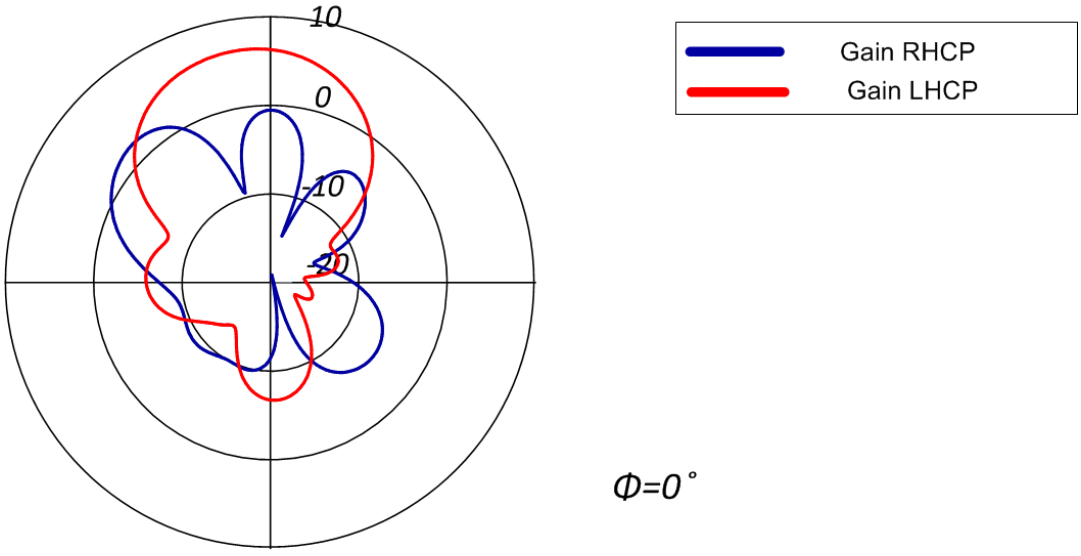

Figure 71: Radiation Pattern for Sum Configuration folding inward 40˚

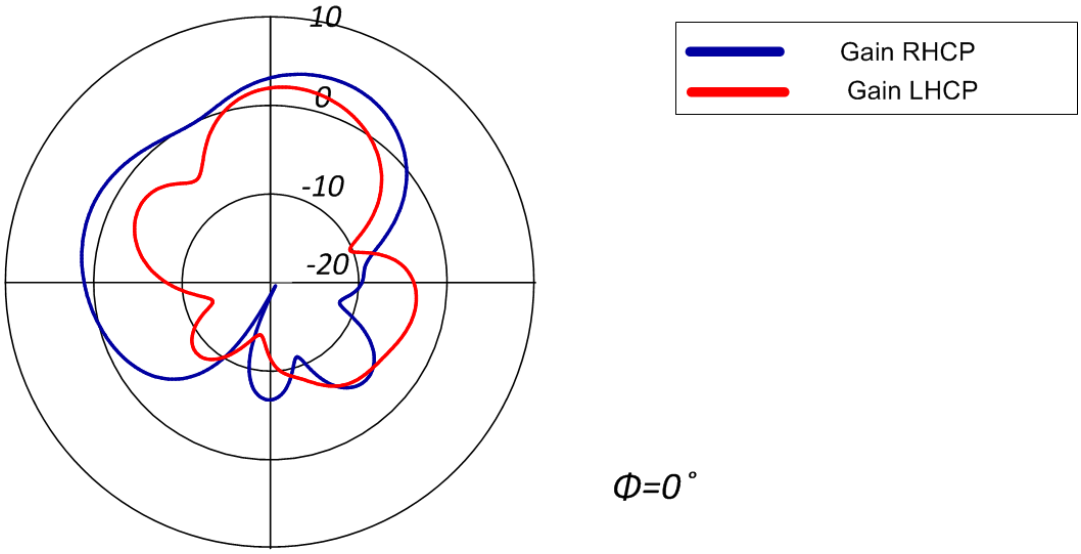

Figure 72: Radiation Pattern for Sum Configuration folding inward 60˚

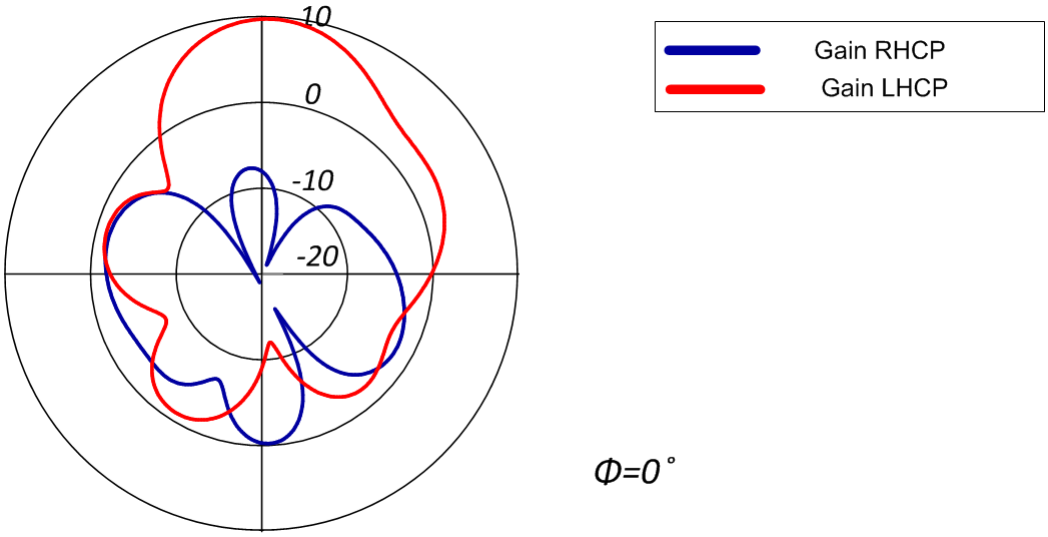

Figure 73: Radiation Pattern for Sum Configuration folding outward 20˚

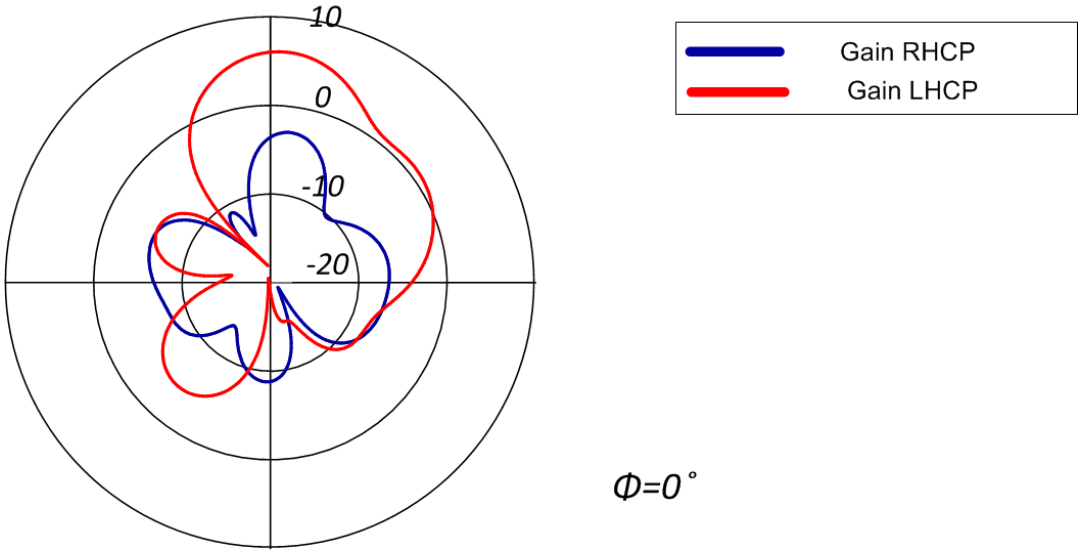

Figure 74: Radiation Pattern for Sum Configuration folding outward 40˚

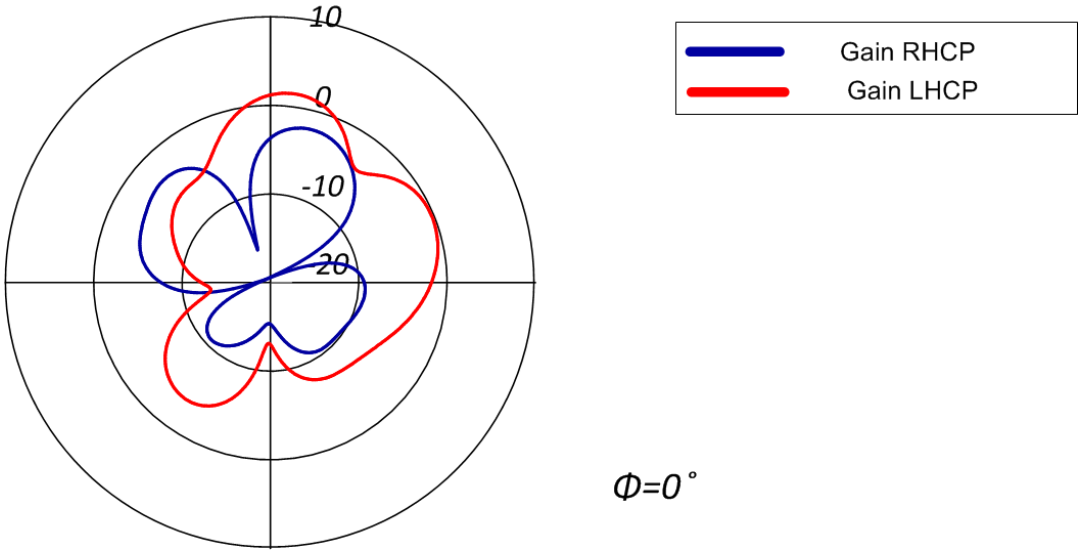

Figure 75: Radiation Pattern for Sum Configuration folding outward 60°

7. SUMMARY

The rectangular patch array is simulated in Comsol and it is observed that with increase in bend angle, the impedance match of the array becomes poor and the beamwidth and gain of the radiation pattern decreases. This is due to the additional loading and mutual coupling between the elements.

The circular patch array is fabricated for the flat configuration for both the sum and the difference configurations. The sum pattern is achieved by using a 180˚phase shift to the adjacent elements of the array. The difference pattern is achieved without any phase shift to the elements. It is observed that as the bend angle increases, the beamwidth increases and the gain or directivity decreases. This can be attributed to the mutual coupling between the array elements. Also, the impedance match of the array becomes poor with the increase in bending. Folding the array outward provides a better impedance match and radiation characteristics compared to folding the array inward.

It is seen that the gain of the array in the sum configuration decreases from 10.24 dB to 4.77 dB as the bending increases from 0˚to 50˚. Also, the difference between the LHCP and RHCP decreases, indicating the loss of the circular polarization which is strongly exhibited at lower angles.

For the difference configuration, a similar trend can be observed. The maximum gain is at $\theta = 30^{\circ}$ and it is 7 dB for 0˚and decreases to 1.63 dB for 50˚. Similarly, the circular polarization reduces. The shape of the pattern also experiences a distortion. Thus, it can

be concluded that the array can be used with same characteristics upto a bend angle of 40˚.

The design considerations that need to be considered while designing an origami array include edges to have less conductor overlapping as this result in ease of folding. The polarization should be circular polarization as this eliminates the need to look at polarization changes as the array is folded.

Origami arrays can be fabricated using shape memory polymers (SMP) and flexible conductors. The SMP enable the array to fold based on an external stimulus like heat and light. These arrays can be fabricated in a laser or 3D printer and the metal can be laser etched on the surface.

REFERENCES

[1] Steven Gao, Qi Luo and Fuguo Zhu, Circularly Polarized Antennas, Wiley 2014.

[2] Constantine A. Balanis, Antenna Theory Analysis and Design, Third Edition, Wiley 2014.

[3] Steven R. Seiler et.al, Physical Reconfiguration of an Origami-Inspired Deployable Microstrip Patch Antenna Array, IEEE AP-S 2017.

[4] K. Miura, Method of packaging and deployment of large membranes in space, Proceedings of 31st Congress International Astronautical Federation, pp. 1-10, 1980.

[5] Mark Schenk, Simon D. Guest, Geometry of Miura-folded metamaterials, Proceedings of the National Academy of Sciences, vol. 110, no. 9, pp. 3276-3281, February 2013.

[6] M. Irsadi Akul et.al, On Slot-Coupled Microstrip Antennas and Their Applications to CP Operation- Theory and Experiment, IEEE Transactions on Antennas and Propagation, vol. 38, no. 8, August 1990.

[7] Deshpande M.D. and Das N.K., Rectangular Microstrip Antenna for Circular Polarization, IEEE Transactions on Antennas and Propagation, vol. AP-34, no. 5, May 1986.

[8] Keith R. Carver and James W. Mink Microstrip Antenna Technology, IEEE Transactions on Antennas and Propagation, vol. AP-29, no. 1, January 1981.

[9] E. Lier, Improved formulas for input impedance of coax-fed microstrip patch antennas, IEE Proceedings H - Microwaves, Optics and Antennas, vol. 129, issue 4, August 1982.

[10] Stefano Maddio, et. al., A New Design Method for Single-Feed Circular Polarization Microstrip Antenna With an Arbitrary Impedance Matching Condition, IEEE Transactions on Antennas and Propagation, vol. 59, no. 2, February 2011.

[11] Gerard J. Hayes, et. al., Self-Folding Origami Microstrip Antennas, IEEE Transactions on Antennas and Propagation, vol. 62, no. 10, October 2014.

[12] IEEE Standard for Definitions of Terms for Antennas, in IEEE Std 145-2013 (Revision of IEEE Std 145-1993), pp.1-50, March 6 2014.

[13] Jun-Hee Na, et. al., Programming Reversibly Self-Folding Origami with Micropatterned Photo-Crosslinkable Polymer Trilayers, Advanced Materials, Vol 27, pp. 79-85, 2015.

[14] Sharma P.C. and Gupta K.C., Analysis and Optimized Design of Single Feed Circularly Polarized Microstrip Antennas, IEEE Transactions on Antennas and Propagation, vol. AP-31, no. 6, November 1983.

[15] R.Q. Lee et. al., Circular polarization characteristics of parasitic microstrip antennas, Antennas and Propagation Society International Symposium, 1991. AP-S. Digest, June 1991.

[16] Kin-Lu Wong and Yi-Fang Lin, Circularly polarised microstrip antenna with a tuning stub, Electronic Letters, Vol. 34 No. 9, 30th April 1998

[17] Boyon Kim et.al., A Novel Single-Feed Circular Microstrip Antenna With Reconfigurable Polarization Capability, IEEE Transactions On Antennas And Propagation, Vol. 56, No. 3, March 2008

[18] H. Iwasaki et.al., A circularly polarized microstrip antenna using a crossed-slot feed, Antennas and Propagation Society International Symposium, 1990. AP-S. Merging Technologies for the 90's. Digest., May 1990.

[19] P.S. Hall et.al., Design principles of sequentially fed, wide bandwidth, circularly polarised microstrip antennas, IEEE Proceedings, Vol. 136, Pt. H, No. 5, October 1989.

[20] Liang C. Shen, The Elliptical Microstrip Antenna with Circular Polarization, IEEE Transactions On Antennas And Propagation, Vol. Ap-29, No. 1, January 1981

[21] Nasimuddin et.al., Slotted Microstrip Antennas for Circular Polarization with Compact Size, IEEE Antennas and Propagation Magazine, Vol. 55, Issue 2, April 2013

[22] Marc Behl and Andreas Lendlein, Shape Memory Polymers, Materials Today, Vol. 10, No. 4, April 2007

[23] Naoji Matsuhisa, et. al., Printable elastic conductors with a high conductivity for electronic textile applications, Nature Communications 6, Article number: 7461, 2015